UNIVERSITÀ DEGLI STUDI DELL'AQUILA

Department of Civil, Construction-Architectural and Environmental Engineering

Doctoral Thesis

Smart boundary conditions for numerical modeling of hurricane-induced storm surge

Ph.D Course in Civil, Construction-Architectural and Environmental Engineering

XXXVI cycle

Candidate

Ludovico Cipollone

SSD

ICAR/02

Course Coordinator

Professor Marcello Di Risio

Thesis Tutor

Professor Marcello Di Risio

Co-Tutor

Ph.D. Davide Pasquali

Smart boundary conditions for numerical modeling of hurricane-induced storm surge

Ludovico Cipollone

Professor Marcello Di Risio

Ph.D. Davide Pasquali

Smart boundary conditions for numerical modeling of hurricane-induced storm surge

Ludovico Cipollone
Candidate ID number: 275112

Department of Civil, Construction-Architectural and Environmental Engineering-DICEAA
University of L'Aquila

Website: http://diceaa.univaq.it/

It's like in the great stories, Mr. Frodo. The ones that really mattered. Full of darkness and danger they were, and sometimes you didn't want to know the end, because how could the end be happy? how could the world go back to the way it was when so much bad had happened? But in the end, it's only a passing thing. This shadow, even darkness must pass. A new day will come, and when the sun shines, it will shine clearer. Those were the stories that stayed with you, that meant something. Even if you were too small to understand why. But I think, Mr. Frodo, I do understand. I know now. Folk in those stories had lots of chances of turning back, only they didn't. They kept going because they were holding on to something. There's some good in this world, Mr. Frodo, and it's worth fighting for.

Abstract

Tropical cyclones (hereinafter referred to as "cyclones" or "hurricanes") are among the most intense weather systems observable in our atmosphere. When they approach coastal areas, they can induce significant storm surges. The increasing intensity of tropical cyclones and attention to phenomena related to climate change raise the hazard associated with coastal areas and make it crucial to update warning systems. For the study of storm surge induced by tropical cyclones, the use of specific numerical models is fundamental. While these models can reproduce the physics of the phenomenon and its effects, they require high computational costs. This cost could be reduced by decreasing the size of the calculation domain, but the results of numerical simulations are strongly influenced by boundary conditions. Reducing the size of the calculation grid, given the complexity of the phenomenon, would lead to defining unreliable boundary conditions and consequently unreliable final results. With this premise, this work aims to propose a novel approach for studying storm surge induced by hurricanes. Subsequently, the results from this model would be used to perform detailed numerical simulations. In this way, large-scale effects that would not be reproducible by reducing the size of the calculation grid would be taken into account through the application of appropriate boundary conditions. The analytical model is formulated by applying the theory of linear systems. It relies on the definition of a response function to an instantaneous pressure field, then applying the convolution integral to obtain an impulsive response function. Subsequently, the principle of superposition of effects is applied to reproduce the actual effect of a cyclone. To define the pressure field produced by a hurricane, reference will be made to a specific parametric model of wind and pressure.

Finally, to assess the actual reliability of the model, it is validated through numerical simulations.

Contents

List of Figures

List of Tables

Introduction

Chapter abstract

In this chapter the main aspects of tropical cyclones, as structure and formation are discussed. Later extratropical cyclones, particularly Mediterranean hurricanes are introduced. Cyclone-induced storm surge is described in terms of the main impact it has on the coastal zone, and how it can be studied and forecasted. Some bibliographic contributions are reported and highlighted so that the main aspects that inspired the proposed model are discussed. In the end, work objectives and features of the proposed method are presented.

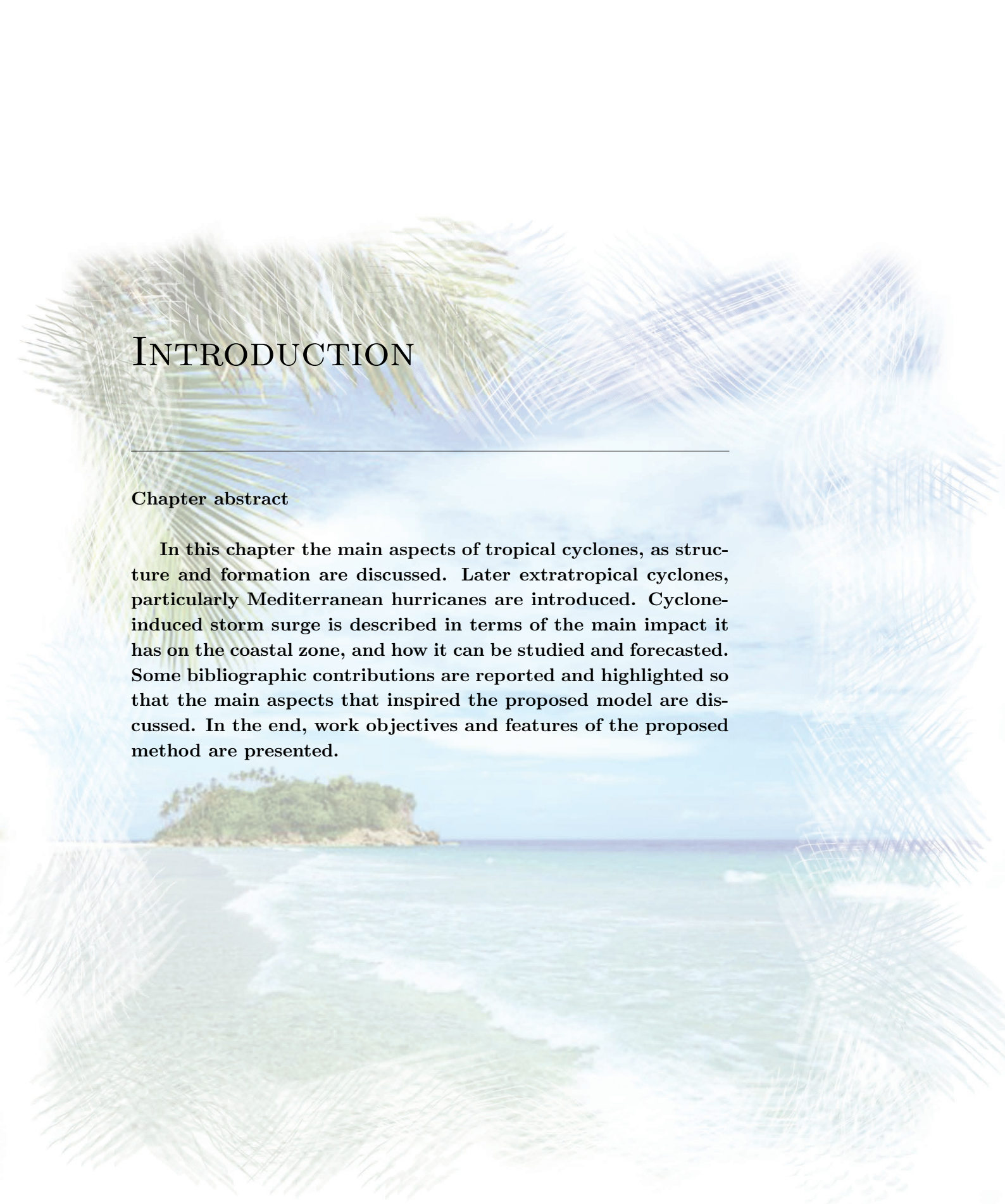

1.1 Tropical Cyclones

Tropical cyclones are swiftly rotating storm systems distinguished by a central area of low pressure, a closed circulation in the lower atmosphere, powerful winds, and an organized pattern of thunderstorms that result in intense rainfall and gusty winds [WaNg (2012)]. The term "Tropical" denotes the geographic source or origin of these systems while the term "Cyclone" describes the circular movement of winds, swirling around the clear central eye of the storm.

Tropical cyclones are known by different names depending on the region they form. In the Indian Ocean are referred to as cyclones, in the western Pacific are referred to as typhoons, in Australia as Willy Willies while in America are referred to as hurricanes.

Tropical cyclone formation requires many atmospheric conditions, thermodynamics, and the role of various meteorological factors [Montgomery and Farrell (1993)] as:

- Ocean-Atmosphere Interaction;
- Low-Pressure System Development;
- Formation of an atmospheric disturbance;
- Cyclonic Spin;
- Eyewall and Eye Formation.

1.1.1 Tropical cyclone formation

Tropical regions receive most solar radiation from direct sunlight rays produce more intense heating. So in tropical areas, warm air rises, creating a low-pressure zone. This rising air then moves poleward and cools as it ascends. As the air cools, it descends around 30 degrees latitude north and south of the equator, forming high-pressure zones known as subtropical high-pressure belts. The descending air returns to the surface and flows back toward the equator, completing the Hadley Cell. This circulation pattern dominates the tropics and subtropics. In mid-latitudes (between

30 and 60 degrees latitude), the Ferrel Cell exists. It involves the interaction of the rising air from the subtropics with the descending air from the polar regions. The polar cell operates near the poles, with cold air sinking and moving toward lower latitudes at the surface. These cells work together to transport heat poleward and help balance the Earth's energy budget. Since Hadley and Ferrel Cells individuates a High-pressure zone at 30 degrees latitude, high and low-pressure system interacts generating wind fields.

Surface winds blow counterclockwise in the Northern Hemisphere and clockwise in the Southern Hemisphere due to the Coriolis effect [Chan (2005)]. The powerful rotating winds in a tropical cyclone occur because of the conservation of angular momentum, which is influenced by the Earth's rotation as air moves inward towards the rotation axis [Smith et al. (2011)].

As described by Tory and Frank (2010), tropical cyclones tend to form over summer, when ocean waters have surface temperatures of at least 26.5 °C. The warm sea surface heats the air above, causing it to become lighter. Since the air temperature rises, a localized low-pressure system at the surface is formed so that new cold air is drawn. The rising air contains huge moisture coming from the evaporated water on the surface. While rising air cools, condenses, and forms a huge cloud. At the same time, the cold air drawn in by the low-pressure system warms up and evaporates, sustaining the entire process. Due to the high moisture cloud becomes thick and heavy so condensation releases the latent heat energy stored in the water vapor providing the cyclone with more power. In these conditions, clouds can grow up to 12-15 km high. As the air moves toward the low-pressure center, it initiates rotation through the preservation of angular momentum, influenced by the Coriolis effect. As the tropical cyclone strengthens, an eyewall develops encircling the center, marked by vigorous convection and the most powerful winds. Within this eyewall, there exists a region of relatively tranquil conditions known as the eye, associated with subsidence and clear skies. Pre-existing atmospheric disturbances, such as easterly waves, and clusters of thunderstorms, often help the formation process of this kind of phenomenon. On the other hand vertical wind shear negatively affects tropical cyclone intensification by displacing moisture and heat from

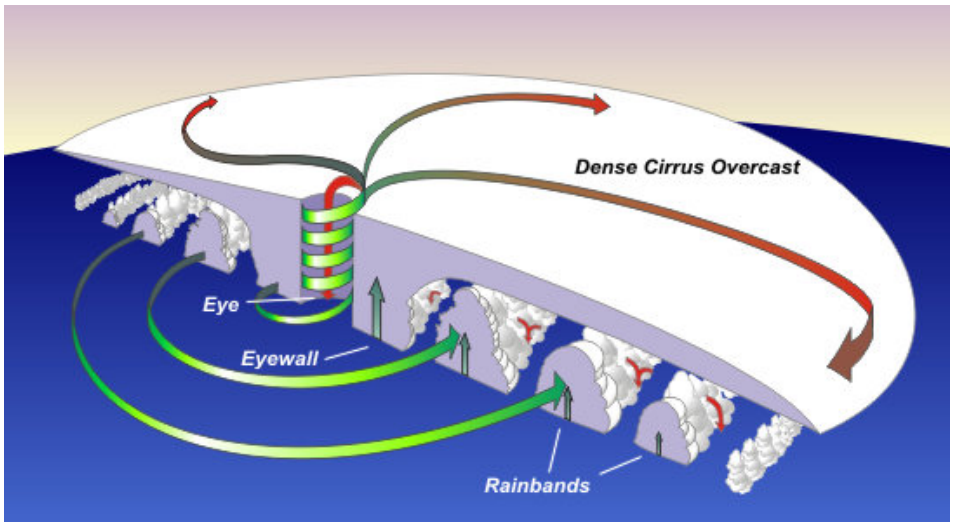

Figure 1.1. Tropical cyclone structures (image courtesy of NOAA)

a system's center.

General tropical cyclone structure is depicted in figure 1.1.

It has also been observed that these phenomena are not unusual in the Extratropical and Mediterranean area and they are referred to as Mediterranean tropical-like cyclones, often referred to as Mediterranean cyclones or Mediterranean hurricanes, and informally as medicanes [Tous and Romero (2013)].

Despite many common aspects with tropical cyclones, Mediterranean cyclones form in slightly different conditions. Medicane tends to not form during summer and do not form in regions where the sea surface temperature exceeds the empirically determined threshold of 26.5 °C, typically associated with tropical cyclones. Also vertical wind shear positively affects the formation process because of the meteo instability that cold wind can cause [Cavicchia et al. (2014)].

The most recent events are the Medicane "Ianos" and "Apollo". Ianos formed on September 16th 2020 east of Sicily, strengthening over the Ionian Sea on the 17th, heading towards Greece where it struck the islands of Cephalonia, Zakynthos, and Ithaca, causing flooding along the western coast of the Peloponnese. Ianos was characterized by a minimum pressure of 984 hPa and associated winds of 120 km/h [Zekkos et al. (2020)]. The medicane Apollo formed, taking on the classical shape of a tropical cyclone, on October 28, 2021, before making landfall on the shores of Catania,

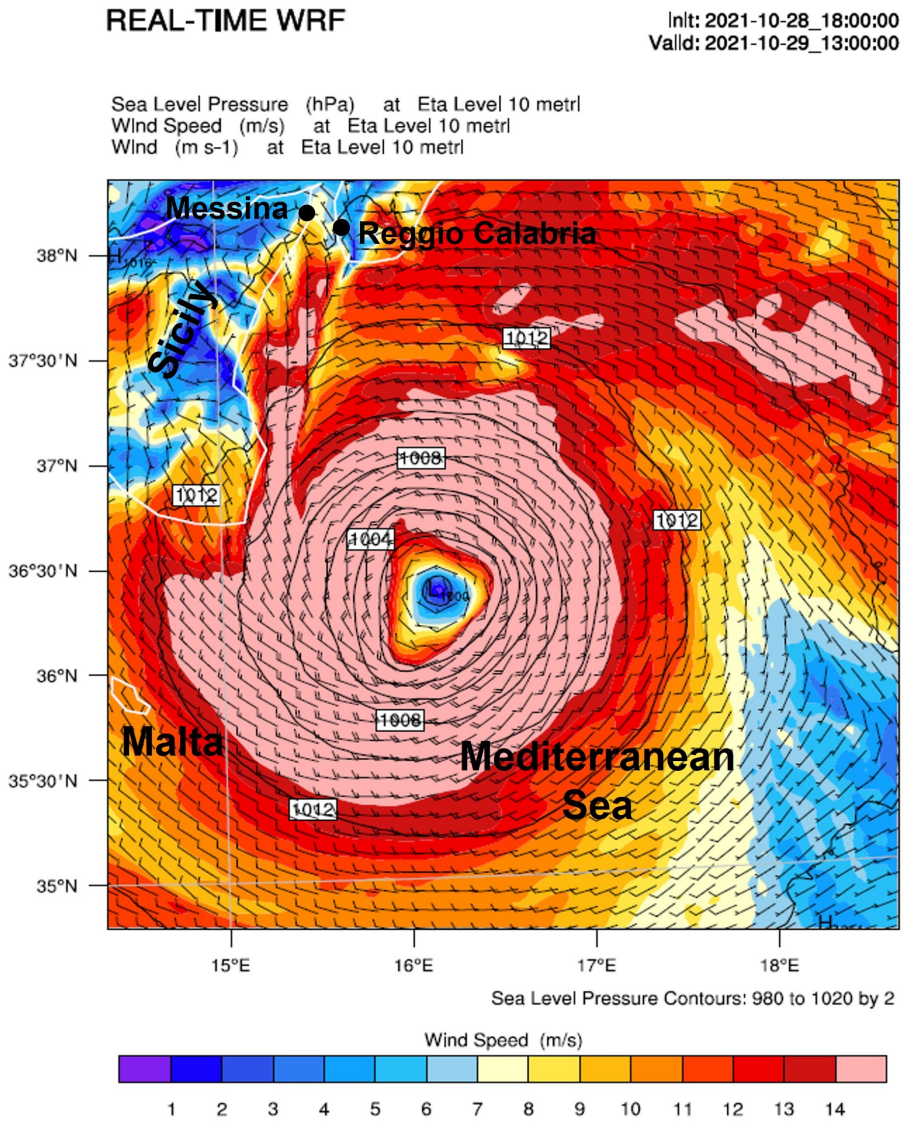

Figure 1.2. An example of the computed wind field and sea level pressure of the "Apollo" Mediterranean hurricane occurred on 29/10/2021 at 13:00 UTC

Sicily, causing floods and three casualties on October 29. Apollo produced a peak wind speed of 104 km/h (65 mph) and a pressure of approximately 999.4 mb [Lagasio et al. (2022)]. In figure 1.2 is shown a snapshot of the Medicane Apollo pressure and wind fields obtained by performing a meteorological simulation using the WRF model [Mylonas et al. (2019)] using GFS reanalysis data [Decker et al. (2012)]. The simulation has been performed by implementing a triple nested grid with a resolution equal respectively of 30, 10, and 3.3 km. Time resolution has been set to 60 seconds while the simulation time starts on 28/10/2021 at 18.00 UTC and ends on 30/10/2021 at 00.00 UTC.

1.1.2 Coastal impact of tropical cyclones

Approaching coastal areas, cyclones can lead to environmental damages, coastal defense issues, coastal flooding, and in some cases the loss of human life [Quader et al. (2017)].

From the environmental standpoint cyclone can severely damage the ecosystem, coastal erosion, and destruction of vegetation. An aspect for ecosystem and vegetation is that hurricanes surge onshore can alter salinity by introducing salt to freshwater areas and raising the salinity levels too high for some habitats to withstand. Also, floodwater can interact with various pollutants and while water is retiring contamination can be carried offshore. Coastal defense issues can occur because water level rise can submerge and damage construction such as breakwaters and seawalls. This event can lead to a loss of functionality of infrastructures themself [Esteban et al. (2014)]. Coastal flooding is mainly due to two factors: rain and storm surge. Storm surge is an abnormal rise of sea surface elevation caused by atmospheric forcing, as the wind stress and atmospheric pressure at the sea surface associated with the storm system. The magnitude of the storm surge at a specific location is influenced by factors such as the coastline's orientation relative to the storm track, the storm's intensity, size, and speed, as well as the local bathymetry. Astronomical tides, caused by the gravitational pull of the sun and the moon, must also taken into account. Both rain and storm surges can cause property damage, and infrastructures and cause human loss [McInnes et al. (2003)].

Also, the increase in the intensity of strong tropical cyclones worldwide [Elsner (2020)], and the growing attention on climate change effects, turn the spotlight on this phenomenon. All these factors contribute to the growing attention on climate change effects and suggest an increasing awareness of the broader impacts of human activities on the environment.

One way to manage the risk related to this kind of phenomenon is to implement early warning systems to provide decision-makers with a tool to reduce the exposure of the population [e.g. Alfieri et al. (2012)].

While not being a true first alert system, the first tool used to evaluate damage induced by hurricanes is the Saffir-Simpson Scale (table 1.1) [e.g.Taylor et al. (2010)].

The Saffir-Simpson Hurricane Wind Scale serves as a tool for evaluating and conveying the potential impact of hurricanes. Its primary focus is on categorizing property damage based on sustained hurricane wind speeds, ranging from Category 1 to Category 5. Each category corresponds to a distinct level of destructive potential, offering a quick and intuitive way to gauge the severity of a storm. This feature enhances its utility for emergency preparedness and response, enabling authorities to effectively communicate the urgency and seriousness of an approaching storm to the public.

Category	**Wind (km/h)**	**Damage**
1	119-153	Minimal, primarily to unanchored mobile homes, trees, and shrubbery. Coastal flooding and minor pier damage.
2	154-177	Moderate, with some roofing material, door, and window damage. Trees may be snapped or uprooted. Coastal and low-lying escape routes flood 2-4 hours before arrival of the hurricane center.
3	178-208	Extensive, with high percentage of framed homes will be destroyed. Trees will be snapped or uprooted, power poles downed, and fallen trees blocking roads. Power outages will last weeks to possibly months. Most of the area will be uninhabitable for weeks or months.
4	209-251	Catastrophic, with a high percentage of framed homes will be destroyed, with total roof failure and wall collapse. Fallen trees and power poles will isolate residential areas. Power outages will last for weeks to possibly months. Most of the area will be uninhabitable for weeks or months.
5	252 or higher	Catastrophic, with a high percentage of framed homes will be destroyed, with total roof failure and wall collapse. Fallen trees and power poles will isolate residential areas. Power outages will last for weeks to possibly months. Most of the area will be uninhabitable for weeks or months.

Table 1.1. Saffir-Simpson Hurricane Wind Scale

It should be noted that the Saffir-Simpson scale is, in any case, a partial tool. Firstly, it does not take into account other potentially deadly hazards such as storm surge, rainfall flooding, and site-specific geographical features, such as the slope of the bathymetry and the elevation of residential complexes, where a hypothetical cyclone could impact.

Secondly, it does not consider the multitude of variables that define the cyclone itself.

For these reasons, complex tools, such as numerical models, must be used to better approach these phenomena. Numerical models can be used in many different ways to obtain different results. One way to use them is by applying them to study how the storm surge changes based on specific characteristics of the hurricane.

Irish et al. (2008) used numerical modeling to study how the cyclone's size can influence storm surge observing the Hurricane Katrina (2005), which was classified as a category 3 event by the Saffir-Simpson scale and produced storm surge larger than many previously observed category 5 events. This study was performed by considering an idealized hurricane and by performing numerical simulations within the ADCIRC model. ADCIRC (ADvanced CIRCulation model), is a numerical model used for simulating hydrodynamics, specifically coastal circulation and storm surge. It is widely employed to study the impact of tropical cyclones, hurricanes, and other extreme weather events on coastal areas. ADCIRC is a finite element model that solves the shallow water equations on unstructured grids, allowing it to capture complex coastal geometries and bathymetric features. The model solves these equations numerically, taking into account various factors such as wind forcing, atmospheric pressure, and bottom friction. The numerical simulations results demonstrate that the cyclone's size significantly influences surge levels, particularly on mildly sloping bottoms and for intense hurricanes. The study compares the surge levels of the Hurricane Katrina and the Hurricane Camille, showing that storm size is a pivotal factor in surge generation, contrary to historical beliefs.

Rego and Li (2009) discuss other factors influencing storm surge, such as landfall timing, and forward speed. In particular, the crucial observation is the significant impact of a hurricane's forward speed on coastal flooding. Slower storms result in greater flooded volumes but lower peak surges, while faster hurricanes produce higher surges but flood narrower coastal sections. The research findings suggest that alterations in a hurricane's forward speed can result in volume fluctuations comparable to a shift of one category on the Saffir-Simpson scale, offering significant insights into the dynamics of

coastal surges.

Numerical models can applied to realize specical hindcast and forecast analyses. Westerink et al. (2008) have realised a hydrodynamic model to meticulously represent the critical aspects of storm surge propagation in southern Louisiana, incorporating accurate model forcing and parameterization of physical processes. The attention to this particular location is due to storm surge intensification by the expansive and shallow Mississippi–Alabama shelf, particularly the low-lying delta. The ADCIRC model has been used to implement unstructured grids that extend from the western North Atlantic Ocean to the Gulf of Mexico, and the Caribbean Sea. The model has been validated for hindcasting Hurricanes Betsy and Andrew and accurately simulating storm surge across Louisiana, with a mean peak surge error of 0.43 m for Betsy and 0.27 m for Andrew. Despite the results, there are instances where the model either overpredicts or underpredicts observed storm surges. Because of that the authors suggest three potential areas for enhancement: refining the definition of bathymetric and topographic data in regions with limited information, integrating raised features into the model grid, and including additional processes associated with storm surge generation. Additionally, efforts are ongoing to link ADCIRC with wind-wave models to evaluate the importance of short-crested wind waves in facilitating momentum transfer and surge setup. This becomes especially critical in areas distant from the storm center and during periods before and after peak winds, where the model tends to underestimate water levels.

Hope et al. (2013), similarly to Westerink et al. (2008), performed a hindcast model for hurricane Ike on Louisiana and Texas Gulf Coast. The extensive dataset from Ike has been used to validate models like ADCIRC, SWAN, and WAM/STWAVE against measured data. Particularly ADCIRC effectively captured the surge's growth, peak, and recession in this area and the interaction of strong surface water level gradient, shore normal wind-driven surge, and large wave breaking nearshore. Hindcast studies have been realized even in Bengal Bay. One has been proposed by Bhaskaran et al. (2014). In this work, the authors discuss the utilization of the ADCIRC model to replicate the peak surge and coastal inunda-

tion during the impact of the severe tropical cyclone Thane happened in 2011. Through computational analysis using ADCIRC, the study focused on determining the maximum peak surge and the extent of onshore coastal inundation. The model-calculated peak surge closely aligned with the maximum recorded water level elevation (1.2 m vs. 1.1 m) reported by ICMAM (Integrated Coastal and Marine Area Management). The proposed model results have been revealed very effective in providing crucial information for generating storm surge vulnerability maps and identifying highly vulnerable regions, valuable for coastal authorities. Additionally, the study recommended improving coastal topography, especially in areas with mild beach slopes, as inundation distance is directly influenced by beach slope.

A different approach to numerical model applied to cyclone-induced storm surge is represented by van Ormondt et al. (2021) work in which they presented a novel semi-empirical storm surge prediction (SESSP) method, designed to calculate tropical cyclone-induced storm surge levels. To derive the model the storm surge has been as the sum of five different contributes.: normal, parallel, radial, Ekman, and inverse barometer surge. For each contribution, empirical surge response functions are established based on outcomes from numerous numerical model simulations performed with the DELFT3D-Flow model, simulating synthetic storms at coasts with diverse cross-shore topography. Non-linear fitting procedures are applied to derive surge response functions (SRFs). The SESSP method accurately replicates peak surge levels within a 10 percent margin of values computed by hydrodynamic models. The work reveals varying surge responses at different types of coasts. Steep coasts exhibit a surge dominated by the inverse barometer effect, while along intermediate and mild-sloping coasts, wind set-up plays the most significant role in peak surge. The Ekman surge, influenced by the Coriolis effect, typically peaks several hours before landfall and can contribute either positively or negatively to the peak surge. On mild-sloping coasts, the radial surge gains relatively more significance. SESSP's computational efficiency enables the execution of ensemble forecasts, involving thousands of synthetic storms across extensive coastal areas.

1.2 Aim and motivations of the thesis

What emerges from the analysis of the bibliographic contributions is that numerical modeling has significantly changed the approach to the problem. The ability to take into account bathymetric and topographic data, the presence of rivers, and other site-specific peculiarities, along with addressing the problem through the solution of specific equations describing the phenomena, allows for a very effective description of storm surge phenomena. On the other hand, the expansion of calculation domains and the complexity of the phenomena involved make the numerical models characterized by high computational costs. To reduce it, a possible approach could be to make smaller computational grids.

It should be observed that the definition of reliable boundary conditions is crucial for the reliability of the solution within the computational domain. Indeed, reducing grid dimensions would make the reliability of the solution highly influenced by the reliability of the boundary conditions. Hence, the more reliable the boundary conditions are, the more representative the achieved solution is. It has to be then stressed that the size of the computational domain plays a particularly crucial role in the large-scale phenomena related to Cyclones' path. Because of that, while using numerical models, nested domains are usually adopted. In doing so, first, a large domain simulation with coarse grid resolution is performed and then its results are used as boundary conditions for detailed numerical simulation with smaller grid and finer grid resolution. This approach leads to the performing of two distinct numerical simulations and computational cost could not be reduced enough. Because of that, this research work aims to propose a novel approach able to analytically describe hurricane-induced storm surge (modeling both temporal and spatial variations) useful to define reliable boundary conditions to be used within hydrodynamic simulations with reduced domain size, hence reducing the computational costs of detailed numerical simulations. This approach aims to propose a combination of analytical and numerical approaches that are often used to tackle complex problems where numerical details simulations are nested with the results obtained by using the proposed analytical method. In particular,

the analytical relies on dynamical system theory [Kalman (1963)]. Doing so it is possible to describe free surface elevation by using an instantaneous response function to a pressure field input mathematically expressed using a Dirac delta function [Di Risio et al. (2017)]. Then it is possible to use convolution integral to obtain a response function to a finite duration impulse [Pasquali et al. (2019)]. At last superposition of effect can be applied to consider multiple impulse action and cyclone translation velocity can be considered.

The proposed approach

Chapter abstract

In this chapter the proposed analytical model is formulated. The proposed method relies on the theory of dynamics of linear systems so that it is possible to evaluate free surface elevation in terms of a response function to the pressure field. First, the instantaneous response function has been found, and then, by applying convolution integral a finite duration response function has been obtained. Then superposition of effect is applied so that the continuous action of the cyclone induced pressure field will be described as a succession of finite duration impulses occurring in different locations at different instants. To describe the actual cyclone pressure field the Holland parametric wind-pressure model will be used.

2.1 General characteristics of the proposed approach

Mathematical models are a set of relationships and/ or mathematical laws that can capture most of the characteristics of a phenomenon. Mathematical models can be either analytical or numerical.

Analytical modeling involves finding exact, closed-form or integral, clear, and concise solutions to mathematical equations. These solutions are often expressed in terms of mathematical functions. Often this approach requires making simplifying assumptions to solve equations, which may limit the model's applicability in capturing real-world complexities. Numerical modeling involves obtaining approximate solutions through numerical methods, such as algorithms and simulations. These solutions are obtained by performing calculations on a computer and are better suited and adaptable to complex problems where analytical solutions are difficult or impossible to obtain. This approach is more versatile and applicable to a broader range of problems, especially those involving computational fluid dynamics, structural analysis, and other complex systems but requires high computational cost.

As already mentioned in chapter 1.2 this work aims to formulate a new approach to predict the free surface elevation induced by cyclones' pressure field. This approach consists of two main steps. The first consists of the analytical formulation of the free surface elevation indued by cyclones' pressure field. The second consists of the application of numerical simulation of the analytical formulation. Since both analytical and numerical model has been cited, the definition of both is required.

The proposed analytical method aims to reproduce the free surface elevation induced by cyclones' pressure field, relying on the theory of linear dynamic systems.

In the context of linear dynamic systems theory, the transient free surface elevation resulting from an instantaneous pressure field can be deduced through the instantaneous response function. Then, it is possible to evaluate the response of the system to whatever the pressure field is by using the convolution integral, i.e. by applying the superposition of effects principle.

The response function enables the estimation of the system's response to a series of impulses with finite durations, considering their respective locations. The fundamental idea is to characterize the path of the cyclone and the translation velocity by representing them as a sequence of finite-duration impulses happening at various locations and time points.

To do so, first an instantaneous response function must be defined. In the scientific literature, among the many contributors, two main studies describe the free surface elevation induced by pressure disturbances relaying linear dynamical systems, that are Proudman (1929) and Le Méhauté and Wang (1996). Proudman (1929) derive motion induced by varying atmospheric pressure acting normally on the sea using theory of linear dynamic system. On the other hand Le Méhauté and Wang (1996) focused on studying the wave motion induced by underwater explosions. In particular, the wave motion is derived by defining an instantaneous response function of free surface elevation to the pressure field induced by the explosion. Since both formulations use generic mathematical definitions of the pressure field, while using the same approach, Le Mehaute approach is used. To describe the cyclone pressure field the Holland model [Holland (1980)] will be used. It should be stressed that this work aims not to propose a new mathematical tool, since both Le Mehaute and Holland ones have already been accepted among the scientific community. The innovative aspect of the proposed approach consists precisely in using tools already available but applying them to a new case study.

2.1.1 General solution

The analytical formulation can be obtained in a cylindrical reference frame r, z (with z being the vertical coordinate and r the radial coordinate). Assuming that the fluid is incompressible (ρ_w = costant, being ρ_w the fluid density) and the flow is irrotational, the velocity field can be expressed by resorting to the definition of a scalar function (the velocity potential, Φ):

$$\vec{v} = \{v_r, v_z\} = \nabla\Phi(r, z, t) \tag{2.1}$$

where v_r and v_z are the components of local velocity in the cylindrical reference frame (i.e. radial and vertical respectively) and ∇ indicates the gradient operator. Since the motion is assumed irrotational defining a potential function allows to define the free surface elevation function $\eta = \eta(r,t)$. Using a nondimensional method leads to mathematical variables as in equations (2.2), where g is the gravity acceleration, V is the velocity, σ is the frequency, p is the pressure, and d is the depth.

$$\begin{aligned} r^*, z^*, \eta^* &= \frac{(r,z,\eta)}{d} \\ t^* &= t\sqrt{\frac{g}{d}} \\ V^*(v_r, v_z) &= \frac{V(v_r, v_z)}{\sqrt{gd}} \\ p^* &= \frac{p}{\rho g d} \\ \sigma^* &= \sigma\sqrt{\frac{d}{g}} \\ \phi^* &= \frac{\phi}{d\sqrt{gd}} \end{aligned} \tag{2.2}$$

From now on, notation with the asterisk (i.e. dimensionless variables) has been eliminated. Then, the governing equation is the Laplace equation becomes

$$\nabla^2\phi = \phi_{zz} + \phi_{rr} + \frac{1}{r}\phi_r \tag{2.3}$$

Respectively, kinetic ad dynamic free surface boundary conditions are

$$\begin{aligned} &\phi_z = \eta_t \qquad\qquad \text{at } z = \eta \cong 0 \\ &\phi_t = -\eta - p \end{aligned} \tag{2.4}$$

Kinetic boundary condition on bottom is written as it follows

$$\phi_z = 0 \qquad \text{at } z = -1 \tag{2.5}$$

Since the problem is described by a partial differential equation, it is useful to reduce it to linear ordinary differential equations involving several independent variables. Every variable can be found by solving problems

each of which involves one variable only. This method is called the separation of variables and leads to defining the original unknown as a product of new unknowns in the form of $u(x, y) = X(x)Y(y)$. This is possible when a finite domain is considered and boundary conditions are given in curves described by a single coordinate. The general solution is shown in equation (2.6).

$$\phi(z, r, t) = F(r)G(z)[Asin(\sigma t) + Bcos(\sigma t)] \tag{2.6}$$

General solutions of single functions $F(r)$ and $G(z)$ are:

$$F(r) = A_1 J_0(kr) + B_1 Y_0(kr) \tag{2.7}$$

$$G(z) = A_2 e^{kz} + B_2 e^{kz}. \tag{2.8}$$

Considering function $F(r)$ in (2.7), J_0 e Y_0 are respectively Bessel functions of the first and second kind of zero order. Since Y_0 is not limited for $r \longrightarrow 0$ his contribution is set equal to zero (i.e. $B_1 = 0$). Considering $G(z)$, a solution can be found as follows. Eq. (2.8) can be rewritten as follows:

$$G(z) = A_2 cosh(kz) + B_2 sinh(kz). \tag{2.9}$$

Applying kinetic boundary condition on the bottom, described in equation (2.5),

$$A_2 k sinh(kz) + B_2 k cosh(kz) = 0 \qquad \text{at } z = -1 \tag{2.10}$$

leads to (2.10) so that coefficient B_2 can expressed as shown in equations

$$A_2 k sinh(-k) + B_2 k cosh(-k) = 0 \tag{2.11}$$

$$B_2 = A_2 tanh(k). \tag{2.12}$$

A general solution for $F(r)$ and $G(z)$ can be found in equations (2.13).

$$\begin{aligned} F(r) &= A_1 J_0(kr) \\ G(z) &= A_2 \frac{cosh(k(1+z))}{cosh(k)} \end{aligned} \tag{2.13}$$

$$\phi = J_0(kr)\frac{cosh(k(1+z))}{cosh(k)}[Asin(\sigma t) + Bcos(\sigma t)] \tag{2.14}$$

The general solution can be written as in equation (2.14) where coefficients A_1 and A_2 are included in terms A and B.

$$\phi = \int_0^\infty J_0(kr)\frac{cosh(k(1+z))}{cosh(k)}[A(k)sin(\sigma t) + B(k)cos(\sigma t)]kdk \tag{2.15}$$

Using the dispersion relation (first equation of (2.4)) ϕ can be written as in (2.15). Using the dynamic free surface boundary condition (second equation of (2.4)) η can be written so that the general form of free surface function response to an instantaneous pressure field is defined (hence called instantaneous response):

$$\eta(r,t) = \int_0^\infty J_0(kr[-B(k)\sigma sin(\sigma(t-\tau)) + A(k)\sigma cos(\sigma(t-\tau))]kdk. \tag{2.16}$$

Applying the convolution integral leads to defining the general form of the free surface impulse function response to a finite duration (Δt) pressure field, called $\eta(r,t)_{FD}$ where FD stands for finite duration. The formulation can be found in equation (2.17)

$$\begin{aligned} \eta(r,t)_{FD} &= \int_0^{\Delta t} \eta(r, t-\tau)d\tau = \\ &= \int_0^{\Delta t}\int_0^\infty J_0(kr)[-B(k)\sigma sin(\sigma(t-\tau)) + A(k)\sigma cos(\sigma(t-\tau))]kdkd\tau \end{aligned} \tag{2.17}$$

At this point, a specific approach can be achieved only by defining A(k) and B(k) so the problem consists of defining the initial condition on the water surface.

2.1.2 Holland wind pressure model

In general mathematical term, the spatial distribution of pressure impulse can be expressed as follows:

$$p(r_0) = I(r_0) \qquad \text{in } z = \eta_0 = 0 \tag{2.18}$$

where r_0 is the radial coordinate of the pressure disturbance. The pressure field can be modeled as a Dirac delta since it is instantaneous. To relate the impulse definitions to the potential function at $t = 0$ the dynamical boundary condition on the free surface can be used, leading to:

$$\int p(r_0)\delta dt = \int_{t=0} \phi_t dt = \phi(r_0, 0). \tag{2.19}$$

Since the integral of $sin(x)$ is $-cos(x)$ and $cos(0) = 1$, and the integral of $cos(x)$ is $sin(x)$ and $sin(0) = 0$, the contribution of $A(k)$ must be zero, so that pressure field can be expressed ad in equation (2.20).

$$I(r) = p(r) = \int_0^\infty kJ_0(kr)B(k)kdk \tag{2.20}$$

By applying the Hankel transform B(k) term can be mathematically defined as in (2.21), where R is the maximum radial distance of the pressure disturbance.

$$H_I(k) = B(k) = k\int_0^R r_0 J_0(kr)p(r)dr_0 \tag{2.21}$$

Inserting (2.21) in (2.15) and (2.16) lead to the general mathematical expression of the potential function ϕ and free surface elevation η respectively in equations (2.22) and (2.23).

$$\phi = \int_0^R rkJ_0(kr)p(r)kdr_0 \int_0^\infty J_0(kr)\frac{cosh(k(1+z))}{cosh(k)}cos(\sigma t)dk \tag{2.22}$$

$$\eta(r,t) = \int_0^R rkJ_0(kr)p(r)dr \int_0^\infty J_0(kr)\sigma sin(\sigma t)]dk \tag{2.23}$$

The specific mathematical definition of H(k) depends on the mathematical definition of $p(r)$ that can be provided by using parametric pressure models.

Parametric pressure models are empirical mathematical representations

used in meteorology and engineering to describe the behavior of wind and atmospheric pressure under various conditions, such as tropical cyclones (hurricanes/typhoons), extratropical cyclones, or other severe weather events. These models are employed when detailed information about the specific atmospheric conditions is not available or when a simplified representation is sufficient for the intended analysis. These models typically rely on a set of parameters that can be adjusted based on certain characteristics of the weather or the region of interest.

Holland (1980) model provides an analytical expression for the radial pressure distribution and rotating wind distribution as:

$$p(r_0) = p_c + (p_n - p_c)e^{-\frac{A}{r_0^B}} \tag{2.24}$$

$$V_c = [AB(p_n - p_c)\frac{e^{(-\frac{A}{r_0^B})}}{\rho_a r^b} + r^2\frac{f^2}{4}]^{\frac{1}{2}} - r\frac{f}{2} \tag{2.25}$$

where p_c and p_n are respectively pressure at the cyclone's eye and ambient pressure expressed in hPa, V_c indicates the rotating wind velocity (m/s), r is the radial distance expressed in km from the cyclone's eye, ρ_a is the air density expressed in kg/m^3 and f is the Coriolis parameter. A and B are two scaling parameters. A is measured in km^B and determines the extension of the cyclone radius of maximum wind (RMW), while B is dimensionless and expresses how much the pressure drop concentrates near the RMW. The maximum sustained wind associated with a tropical cyclone is a common indicator of the intensity of the storm. RMW is found within the eyewall at a distance that can be calculated by taking equation (2.25), applying $dV_c/dr = 0$, and neglecting the f contribution since, near the RWM, its contribution is low. This leads to define $RMW = A(\frac{1}{B})$. Inserting this relation into equation (2.25) define the value of the maximum wind as

$$V_m = C(p_n - p_c)^{\frac{1}{2}} \tag{2.26}$$

where $C = \frac{B}{\rho_a e}^{\frac{1}{2}}$ with e being the Nepero number. For A values no range values is given while B lies between 1 and 3.0. Equation (2.24) can be

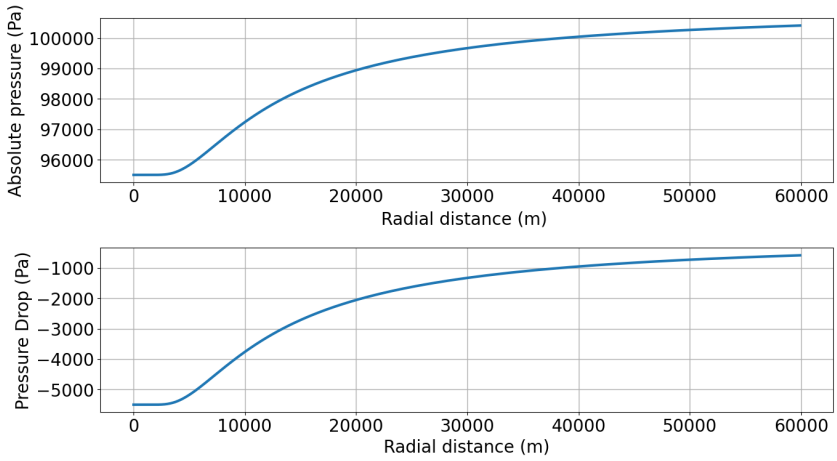

Figure 2.1. Hurricane Tracy pressure field modelled with Holland model ($p_{drop} = 5.5\ kPa$, A=23 km^B, B=1.5. (-)

modified by introducing relative pressure and becoming equation (2.27) where $p_{drop} = p_n - p_c$.

$$p(r) = p_{drop}(1 - e^{-\frac{A}{r^B}}) \tag{2.27}$$

In figure 2.1 is reported the pressure evolution for a the Hurricane Tracy (p_{drop} = 5500 Pa, $A = 23km^B$ and B=1.5 (-) with both equations (2.24) and (2.27).

By inserting the dimensionless pressure field $H_I(k)$ the equations (2.21) split into two addendums called H1 and H2.

$$H_I(k) = H1 + H2 \tag{2.28}$$

$$H_I(k) = p_{drop}\int_0^R r_0 J_0(kr)kdr_0 - p_{drop}\int_0^R r_0 J_0(kr)k(e^{(-\frac{A}{r_0^B})})dr_0 \tag{2.29}$$

Since every variable of the analytical model has been defined, general equations (2.15) and (2.16) have been specialized to their case-specific form in equations (2.22) and (2.23) and they can be solved to study first an instantaneous impulse, then a finite duration impulse and finally applied to a real cyclone-induced storm surge as:

$$\eta(r,t)_{FS} = \int_0^{\Delta t} \eta(r, t-\tau)d\tau = \\ = \int_0^{\Delta t} d\tau \int_0^{\infty} J_0(kr)[H_I(k)\sigma sin(\sigma(t-\tau))dk. \tag{2.30}$$

Instead of the minus sign in equation (2.17), equation (2.30) has a positive sign at the coefficient B(k) since a positive, relative pressure field generates a growth in free surface elevation.

2.2 Numerical integration

Equations (2.21) and (2.30), representing the analytical formulation of the pressure field forcing and the free surface elevation induced by it, can not be analytically solved, so numerical integration must be used. Since a dimensionless approach has been adopted, d is been set equal to 300 m. First, $H_I(k)$ integration is performed by using a Gaussian quadrature algorithm. Gaussian quadrature is a numerical integration technique that works by choosing a set of points x_i (nodes) and corresponding weights, w_i in such a way that the integral of a polynomial of a certain degree is exactly computed. The mathematical formulation is reported in equation (2.31).

$$\int_a^b f(x)\,dx \approx \sum_{i=1}^{n} w_i\, f(x_i) \tag{2.31}$$

The mathematical definition of weights depends on the particular Gaussian algorithm that is used. In this case, Gauss–Legendre quadrature algorithm has been utilized so that

$$w(x) = \frac{2}{(1-x^2)\cdot[P_n'(x)]^2} \tag{2.32}$$

where $P_n^{'}(x)$ is the derivative of the Legendre polynomial of degree n and the $i-th$ Gauss node, xi, is the $i-th$ root of P_n. Legendre polynomials of order 100 have been used.

Beyond the method, equation (2.21) requires the definition of other parameters to be integrated such as p_{drop} and hurricane radial extension. While p_{drop} is immediately definable, hurricane radius R is not since is

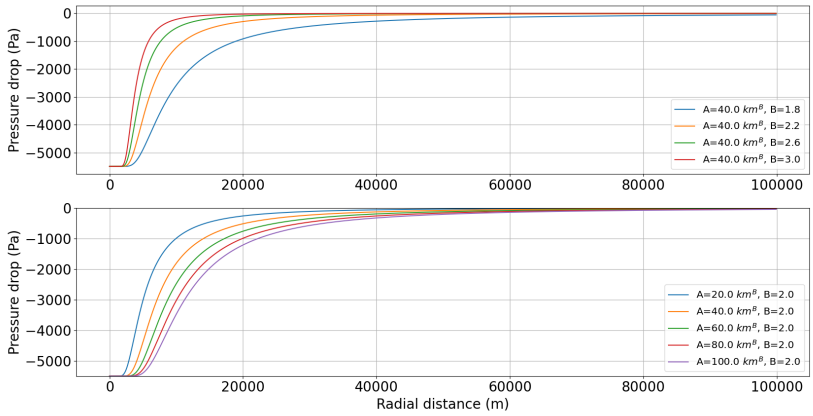

Figure 2.2. Ideal Holland pressure fields used to perform sensitivity analysis.

influenced by the A and B Holland parameters. But since the cyclone geometry changes, it also influences the free surface elevation pattern since different wavelengths and so different values of k must be considered. So sensitivity analysis has been performed by considering many ideal cyclone patterns. In this process, since p_c and p_n represent the initial and the final asymptotic value of the Holland model, p_{drop} is left unchanged and set to 5500 Pa. First, hurricane for a fixed value of A ($A = 40\ km^B$) and various values of B (B = 1.8, 2.2, 2.6 and 3.0) have been considered. The process has been repeated for a fixed value of B (B = 2.0) and various values of A (A = 20, 40, 60, 80, 100 km^B).

Referring to figure 2.2 where all the pressure fields are reported, each cyclone pressure field has been calculated with a spatial resolution of 100 m. The cyclone radius has been estimated as the radial coordinate where pressure is 1% lower than the atmospheric pressure. For fixed A values it is obtained a $R = 100$ for $B = 1.8$, $R = 60$ km for $B = 2.2$, $R = 40$ km for $B = 2.6$ and $R = 20$ km for $B = 3.0$. For B fixed value, changing A does not affect the cyclone radius that for all cases remains 100 km. Being defined the upper end of integration, $H_I(k)$ has been evaluated. As shown in figure 2.3, the smaller B, the smaller k_{max} value must be taken. This happens because, since the physical significance of the B parameter describes, the more B decreases the more the cyclone radius increases, so that longer wavelength must be considered hence a small value of k_{max}. For considered B values it is obtained k_{max} of 1.0, 1.25, 1.50 and 1.75. For

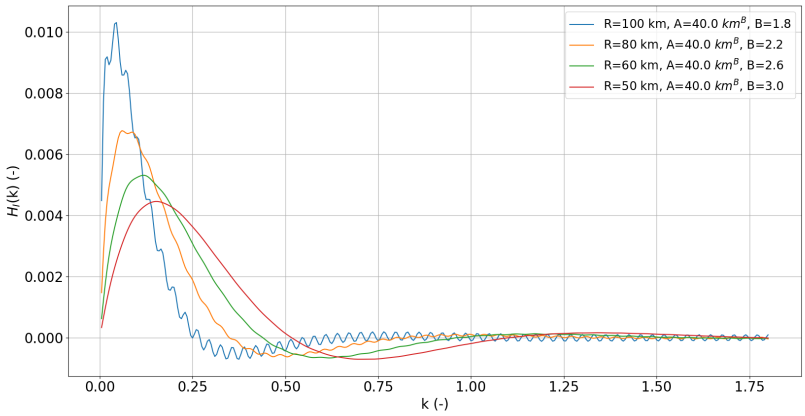

Figure 2.3. k_{max} sensitivity analysis performed with fixed value of A and multiple values of B.

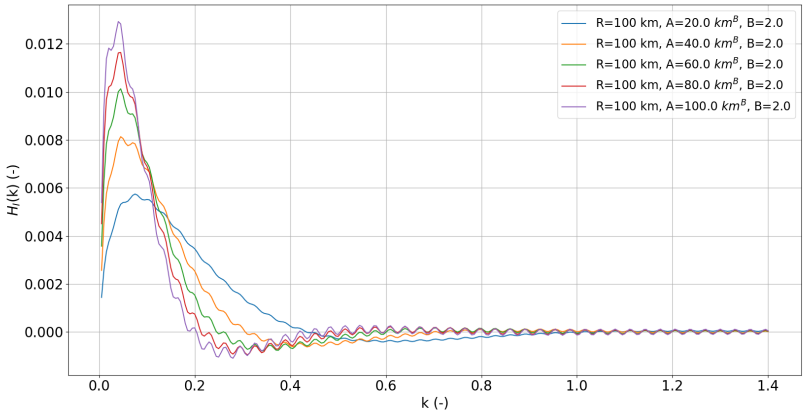

Figure 2.4. k_{max} sensitivity analysis performed with fixed value of B and multiple values of A.

B fixed value, as shown in figure 2.4 since R does not change, neither does k_{max} that can be set as 1.25. Since a numerical approach has been adopted all k values have defined defining the first value, equal to zero, the last value set to k_{max} that is found by performing a sensitivity analysis and a k resolution dk for a pressure field with $A = 40km^B$, B = 2.0 and $k_{max} = 1$. Figure 2.5 shows how for $dk < 0.005$ all curves become overlapping so dk has been set as 0.005.

As equation (2.21), also equations (2.17) and (2.30) have been numerically integrated with a fixed Gaussian algorithm. In both cases, spatial and temporal coordinates must be defined but their resolution and length do not significally affect integral resolution. Also, frequencies must be introduced

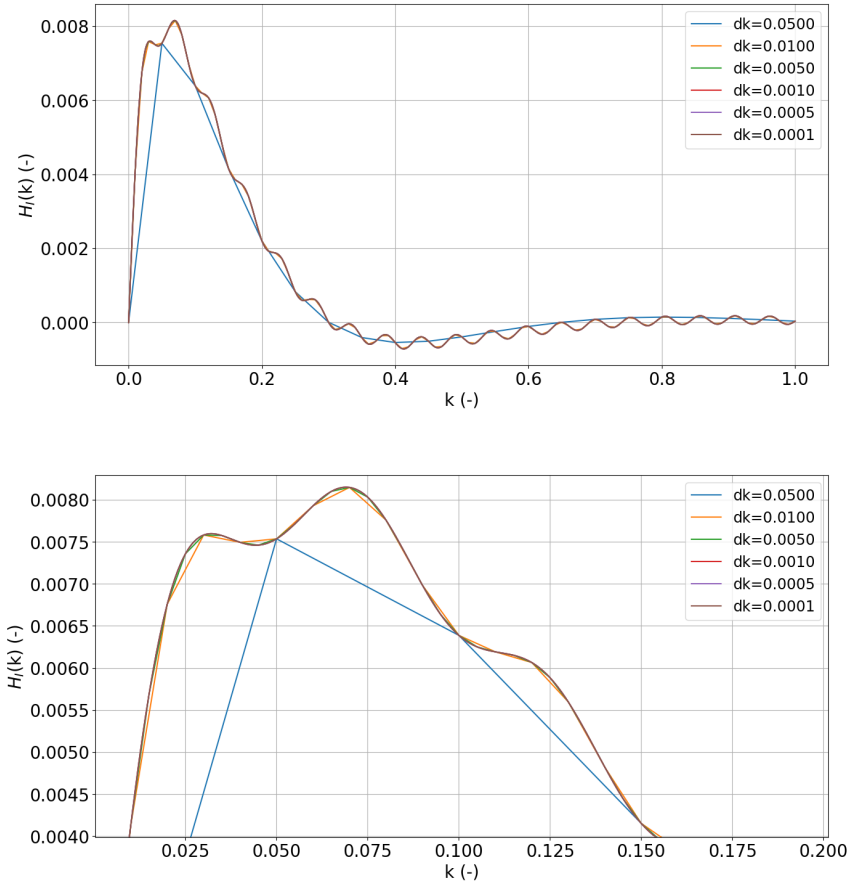

Figure 2.5. dk sensitivity analysis.

and they are defined by applying dispersion relation.

Once the radial and temporal coordinates are defined both in extension and resolution, the function response to a single pressure impulse can be calculated. This process optimizes computational time management since the function response can be calculated once for all time (for the given pressure distribution) and later superposition of effect for multiple applications can be realized both fixed or moving pressure fields (i.e. for moving hurricanes). If impulses fixed in space are considered, radial coordinates can be used. The extension of the radial coordinate has been selected in order to have a negligible wave amplitude at the boundaries. Doing so it is possible to apply a Hanning filter so that the negligible contribution can be set to zero. A Hanning filter, or window, is a mathematical function used in signal processing and it is applied to a time-domain signal, it has the effect of tapering the signal smoothly to zero at its endpoints, minimizing

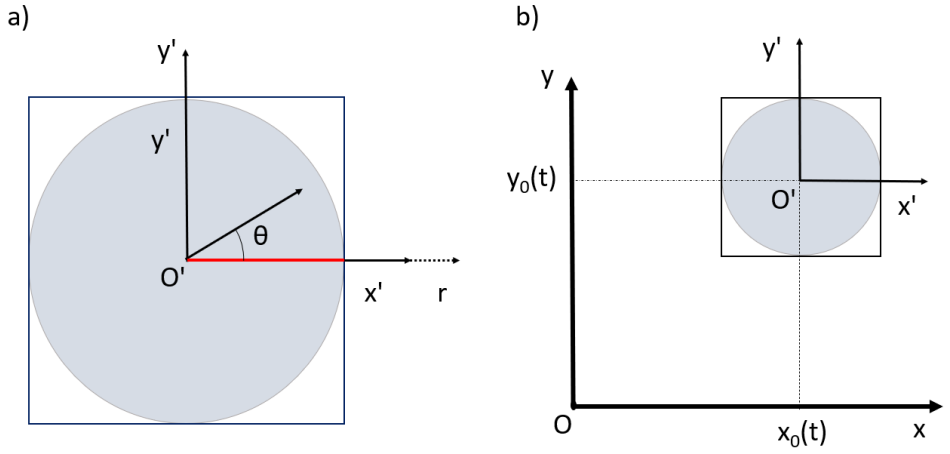

Figure 2.6. Sketch of the radial and cartesian reference frame. The circles represent the cyclone.

abrupt changes. Its mathematical formulation is reported in eq. (2.33)

$$w(n) = 0.5 \left[1 - \cos\left(\frac{2\pi n}{N-1} \right) \right] \tag{2.33}$$

where $w(n)$ is the value of the window at position n, N is the total number of points in the window, and $0 \leq n \leq N-1$. Since a spatial resolution of 1 km has been adopted, the chosen Hanning filter smoothed the wave amplitude for the last 50 points of radial coordinate, equivalent to 50 km. The same procedure is applied for time coordinates too, so that for t_{max} free surface evolution for each point is smoothed leading to zero. When moving finite-duration impulses are considered, further consideration must be made since radial coordinate cannot longer be used. This is due to the fact that the translation velocity of a generic pressure field occurs in an Oxy Cartesian reference frame and is defined by the composition of the velocity components along the x and y axes. Continuing to use the radial coordinate would fail to account for the 2D effects of the phenomenon when the superposition of effects is applied. So, as schematized in figure 2.6, two coordinate transformations must be applied.

The first one allows to write the radial response function in a cartesian system moving with the cyclone (origin located at the cyclone's eye) where θ is the azimuth measured counterclockwise with respect to the x'-axis.

Transformation is applied using equations (2.34).

$$x' = r\cos(\theta) \tag{2.34}$$

$$y' = r\sin(\theta) \tag{2.35}$$

Then, the second one allows to apply the modified response function on a (global) cartesian reference frame:

$$x = x_0(t) + x' \tag{2.36}$$

$$y = y_0(t) + y' \tag{2.37}$$

where $x_0(t)$ and $y_0(t)$ are the cartesian coordinates of the instantaneous location of the cyclone's eye (i.e. representing the path of the cyclone's eye). So operatively, first the already calculated radial response function gets converted in a local Ox'y' coordinate still centered in the cyclone's eye. Then the converted response function gets interpolated on a new global Oxy grid where superposition of effect can be performed taking into account pressure field translation velocity.

2.3 Model application

Since the main aspects of numerical integration have been discussed, the model will be applied to a case study in which the pressure field is defined with $p_{drop} = 5500$ Pa, $A = 40\ km^B$, B=2.2, and R=60 km.

Despite not having a physical meaning, first an instantaneous pressure impulse is considered. Figure 2.7 shows the dimensional instantaneous response function. The free surface elevation reaches its maximum at the cyclone's eye in the early stage of the generation process (a maximum elevation of 6.3 cm has been estimated). As the time elapses, the generated wave propagates with a maximum elevation of the crest still in the order of centimeters. As expected, the observed wave celerity is close to the celerity of long waves, i.e. waves propagating in shallow-water conditions ($\simeq$ 50 m/s).

When a finite duration impulse is considered multiple Δt can be considered and and t_{max} calculated as a Δt multiple. Radial coordinate extend

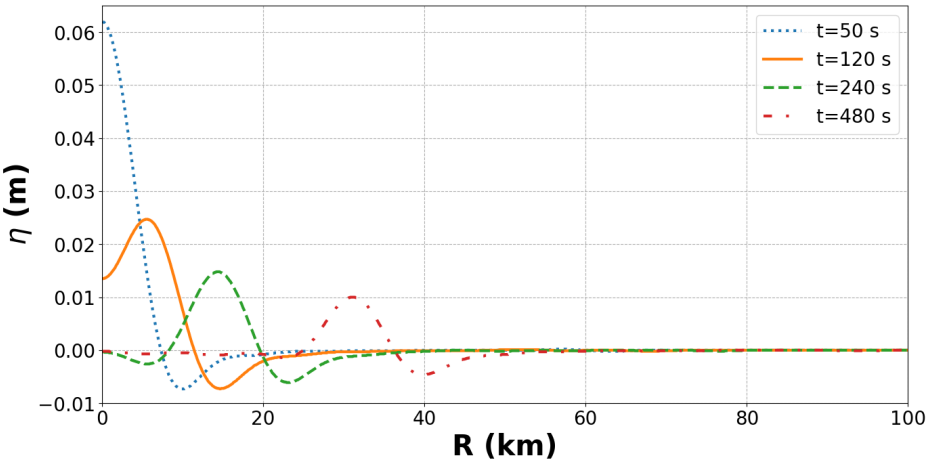

Figure 2.7. Time snapshot of the instantaneous response function calculated with$A = 40\ km^B$, B=2.2 and $p_{drop} = 5500$.

for 250 km with a resolution of 100 m. First a duration impulse of $\Delta t = 50$ s is considered.

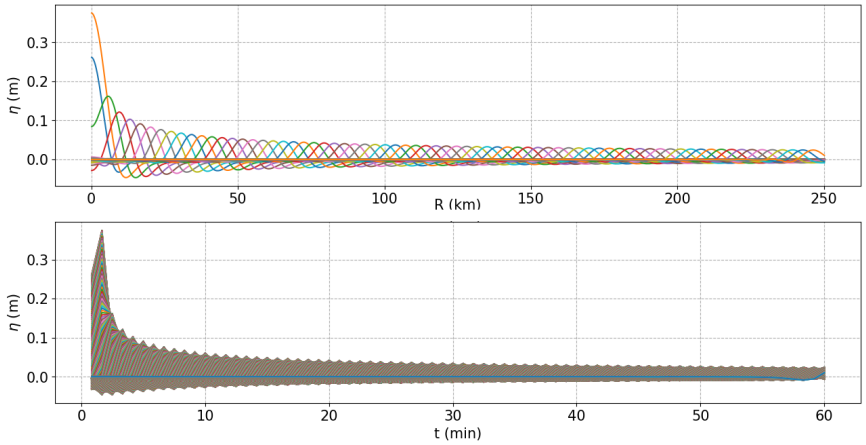

Figure 2.8. Impulse response function calculated for $\Delta t = 50$, A=40 km^B, B=2.2 and $pc_{drop} = 5500$ Pa.

In figure 2.8 the calculated response function is plotted. The first graph shows the temporal evolution of free surface elevation along the spatial coordinate while the second plots the free surface evolution in time for each radial point. It can be seen how both space and time η contribution continues over the considered r_{max} and t_{max}. The Hanning filter application is shown in figure 2.9 and 2.10 where a comparison of the original raw function response and the new windowed response is reported respectively

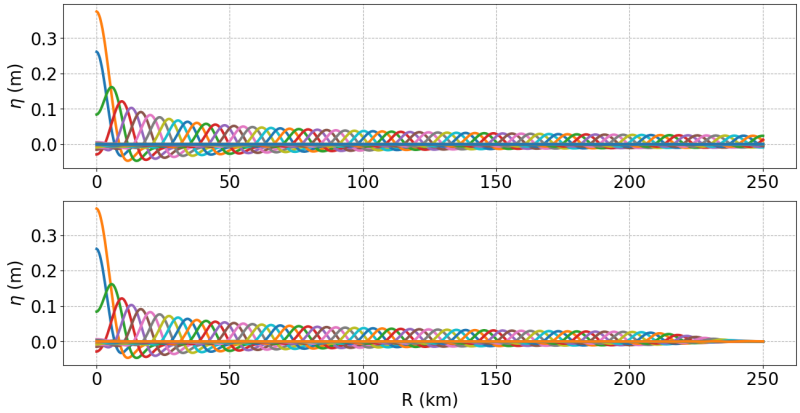

Figure 2.9. Effect of application of Hanning window filter on the response function for radial coordinate.

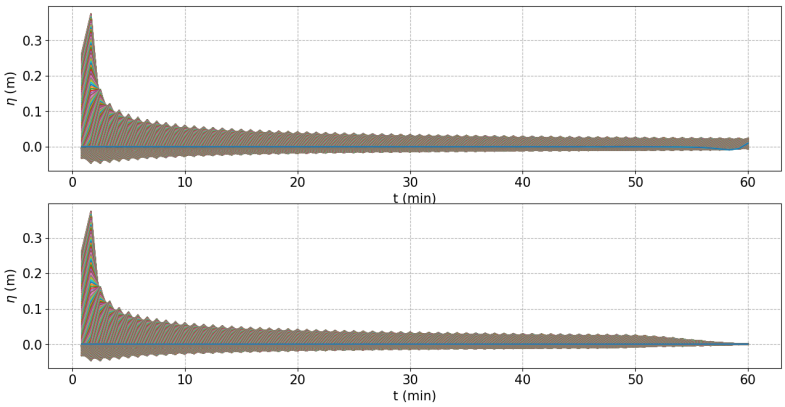

Figure 2.10. Effect of application of Hanning window filter on the response function for time coordinate.

for radial and temporal smoothing.

The new function response can be now applied for study free surface elevation induced by multiple pressure impulses.

In figure 2.11 snapshots of free surface elevation evolution generated by 120 impulses of duration $\Delta t = 50$ s fixed in space are plotted. In the first plot in figure 2.11 is plotted free surface elevation induced by the first 5 impulses. Observing first five snapshots appears clear how free surface elevation is still a transient process since it still changes in time. In the second plot in figure 2.11 is plotted free surface elevation induced by multiple impulses so that η is stationary with a peak elevation of approximately 0.63 cm is obtained. It can also be observed a relatively small in-height

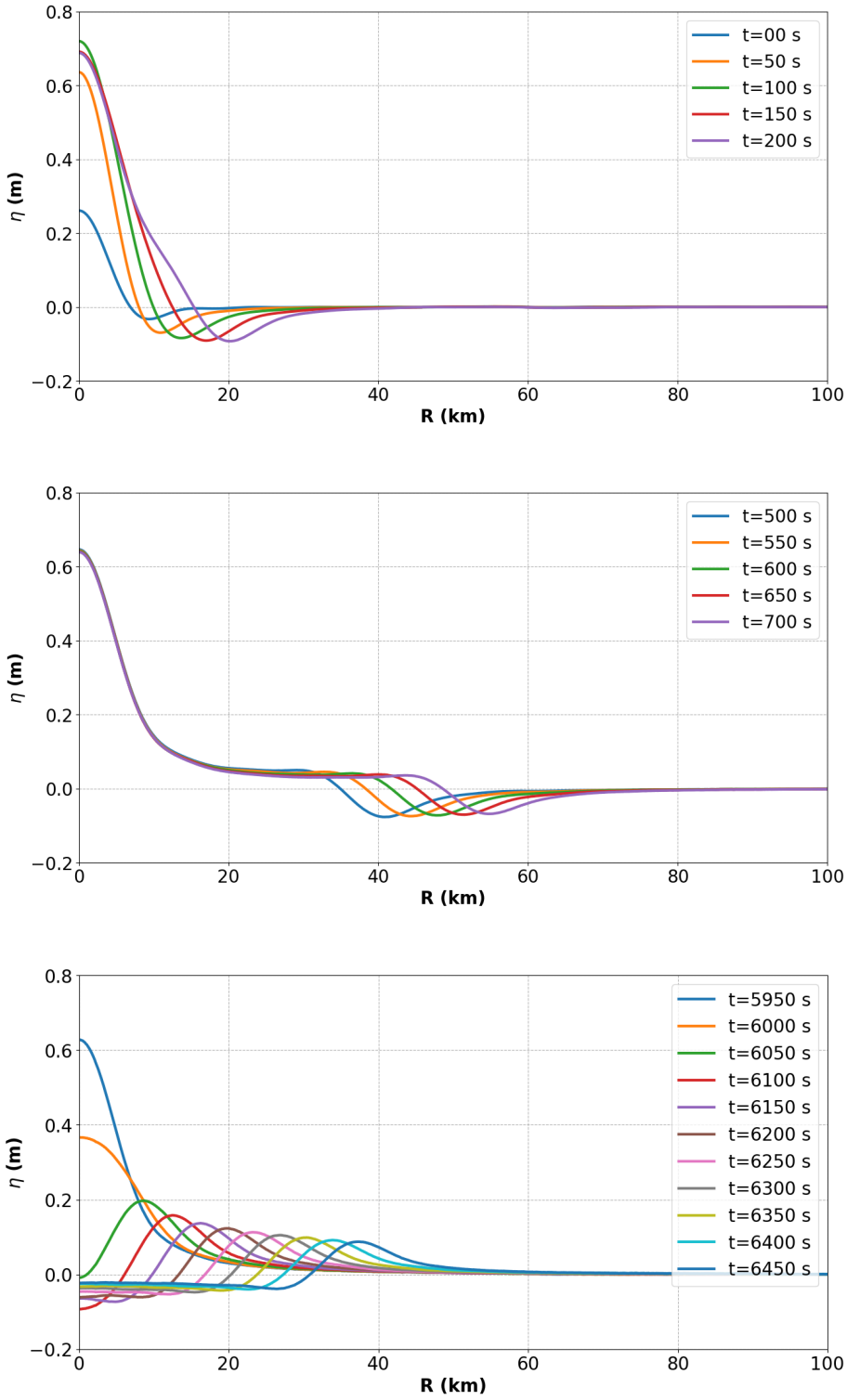

Figure 2.11. Free surface elevation induced 50 fixed pressure impulse of duration 50.

wave propagates along the radial coordinate. In particular, that wave is a disturbance induced by the application of the considered pressure field. In

nature, as also described in chapter 2.3, cyclones need time to completely form. By using this analytical approach it is not possible to replicate the cyclone formation process but its completely formed pressure field is applied on calm conditions. In the third plot in figure 2.11 free surface elevation is plotted while pressure impulses stop to act, starting from $t = 6000$ s. It means that free surface elevation plotted for $t = 50$ s is stationary for all the radial coordinated plotted since the initial disturbance propagates further. When pressure impulses stop, peak elevation suddenly decreases and starts to propagate along the radial coordinate.

To evaluate how well the method proposed performs, superposition of effects can be applied. In this way, as an example, free surface elevation generated by $2n$ impulses of 50 s, fixed in space, is confronted by those induced by n impulses of duration 100 s. The same processes can be repeated for multiple impulse durations. In figure respectively 2.12, 2.13, 2.14 snapshots of comparison of results are reported, and show that errors are in the range of -10^{-4} m and 10^{-4} m.

Also, as in the instantaneous case, the observed wave celerity is close to the celerity of long waves propagating in shallow-water conditions with the amplitude of the crest being an order of magnitude larger than the crest of the instantaneous response function. Also, peak elevation correctly reproduces the inverse baric effect.

2.4 Application of the analytical model to cyclone-induced storm surge

Since the finite duration impulse response function is been evaluated by applying the superposition of effect for fixed impulse, the actual path of the cyclone can be included in the method introducing cyclone translation velocity. As suggested by Ormondt [van Ormondt et al. (2021)] a reasonable range of hurricane speeds of 10 to 40 km/h. The whole cyclone path can be discretized in time as a succession of impulse pressure of duration Δt moving in the space. Indeed, to consider the contribution due to the displacement in space of the pressure field, as also expressed in section 2.2, the radial spatial coordinate cannot be further used. Hence, two co-

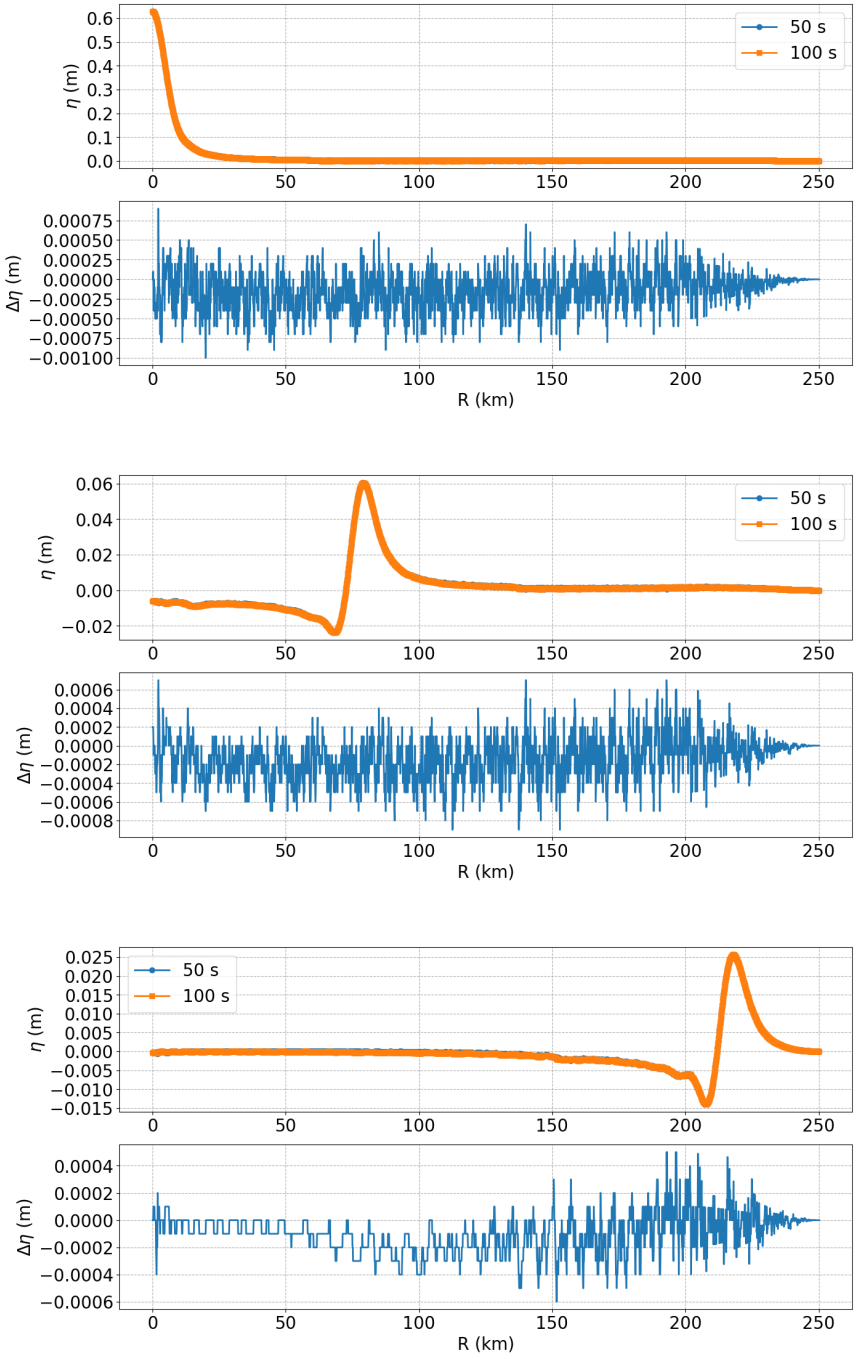

Figure 2.12. Comparison of the free surface elevation generated fixed impulses of duration 50 s and 100 s for t = 4000,7000, 9000 s.

ordinate transformations, described as equations (2.34), (2.35), (2.36) and (2.37) must be applied. Translation velocity is considered by introducing it in the definition of $x_0(t)$ and $y_0(t)$, reported in equations (2.38) and (2.39), that are the cartesian coordinates of the instantaneous location of the cyclone's eye (i.e. representing the path of the cyclone's eye).

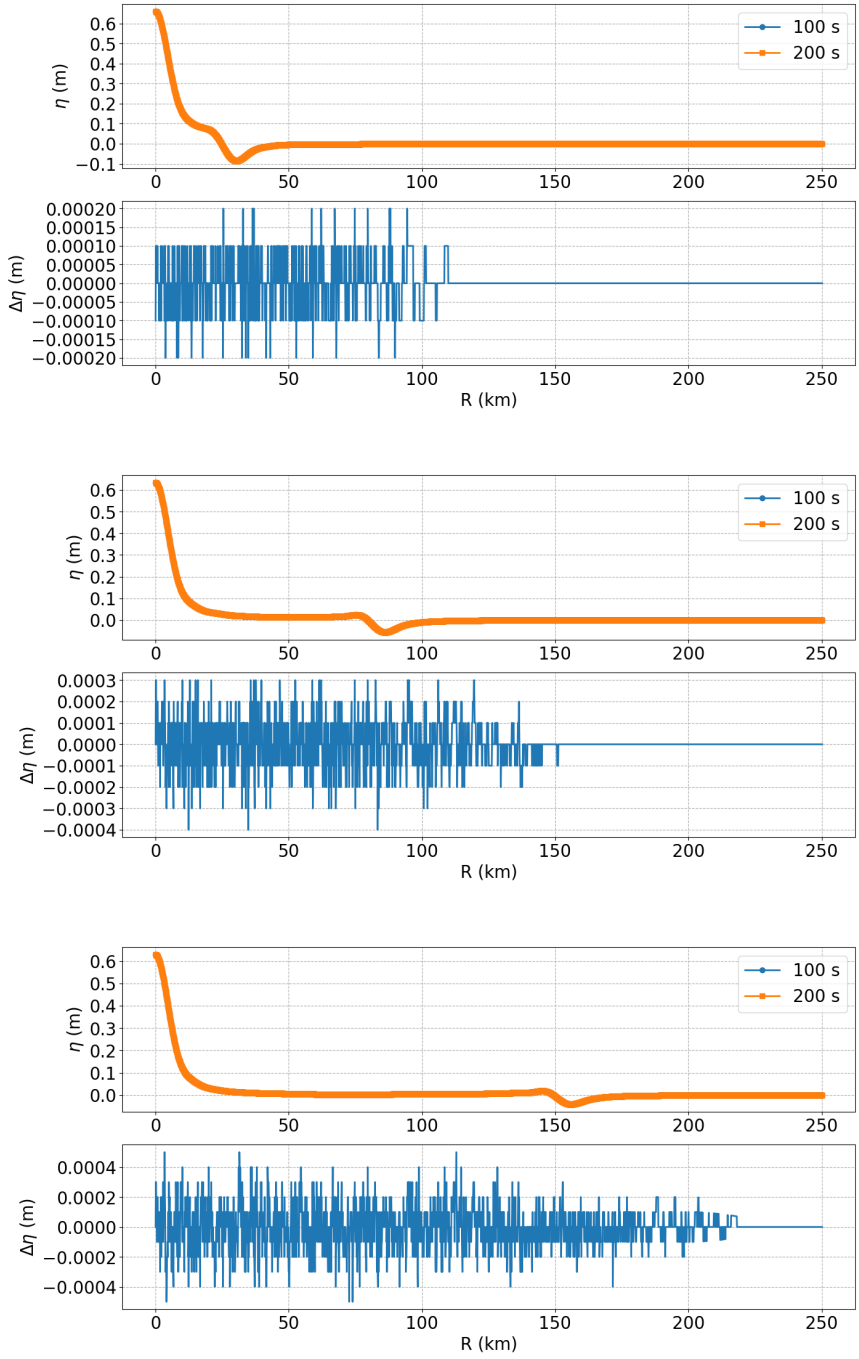

Figure 2.13. Comparison of the free surface elevation generated fixed impulses of duration 50 s and 100 s for t = 200,1000,2000 s.

$$x_0(t) = x_0(0) + \int_0^t V_x(t)dt \tag{2.38}$$

$$y_0(t) = y_0(0) + \int_0^t V_y(t)dt \tag{2.39}$$

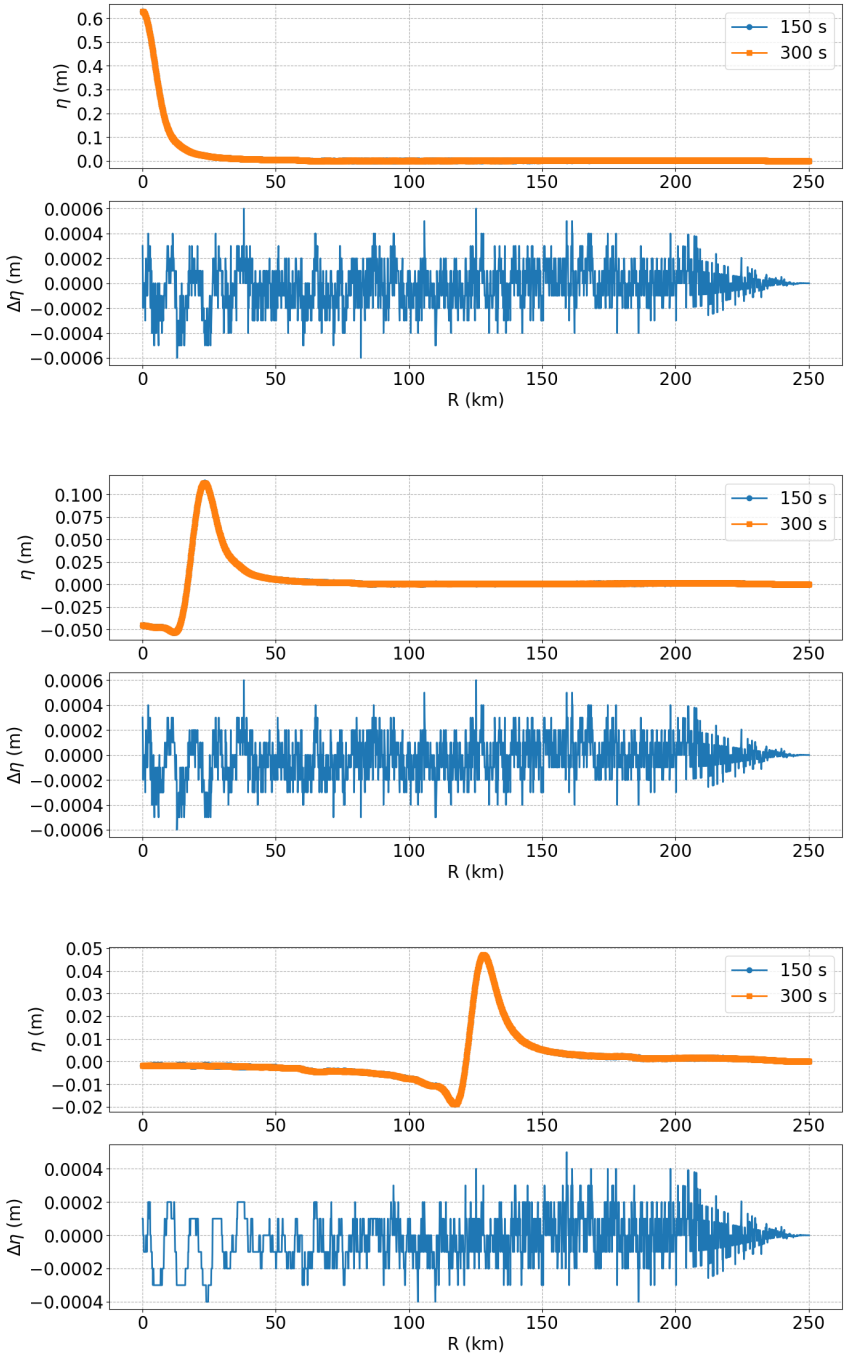

Figure 2.14. Comparison of the free surface elevation generated fixed impulses of duration 50 s and 100 s for t = 6000, 9000, 10500 s.

To map the response function in the reference frame (O',x',y') the response function to a finite duration impulse, calculated in section 2.3 is converted according to the coordinate transformation previously illustrated and then interpolated in a regular structured grid of resolution $\Delta x = \Delta y$. By applying the first coordinate transformation, adopting a grid resolution

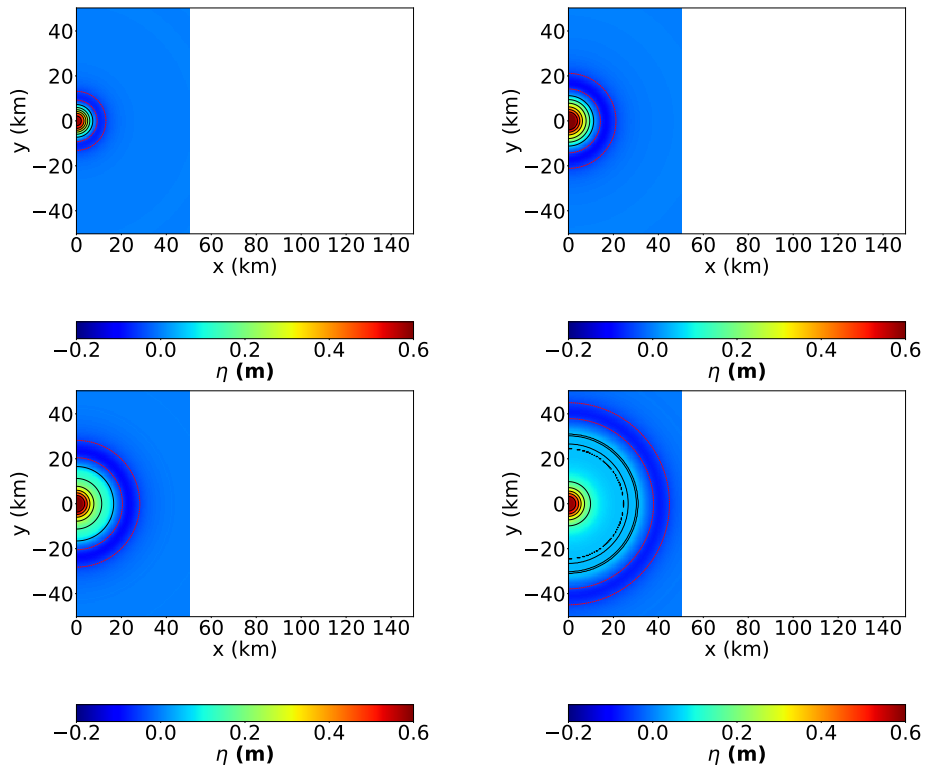

Figure 2.15. Free surface elevation induced by fixed pressure field of duration 50 s, seconds in Cartesian reference frame for t = 100, 500, 1000, 1250 seconds. Contour continuous lines refer to positive levels, contour dashed lines refer to negative levels.

of $\Delta x = \Delta y = 500$ m, considering a single impulse of duration 50 s, snapshots of the free surface are shown in figure 2.15 where x coordinate extend from -50 to 50 kilometers, as y coordinate, and X_0 and Y_0 is equal to zero.

Then, translation velocity is considered, so that the cyclone forward velocity field is $V_x = 35$ km/h and for $V_y = 0$ km/h. In this case, results shown in figure 2.16, are carried out considering a grid with a resolution $\Delta x = \Delta y = 500$m, an x axis that extends from 0 to 150 kilometers, an y axis that extends from -50 to + 50 kilometers and an initial location of cyclone's eye at $X_0 = Y_0 = 0$ km.

As for the fixed pressure field, the model's performance has been tested by comparing, for specific sections, free surface elevation induced by different impulse durations.

Figures 2.17, 2.18, and 2.19 show comparison, at the same temporal instants, between free surface induced respectively by impulses duration of 50 and 100 seconds, 100 and 200 seconds and 150 and 300 s for section $y = 0$ km.

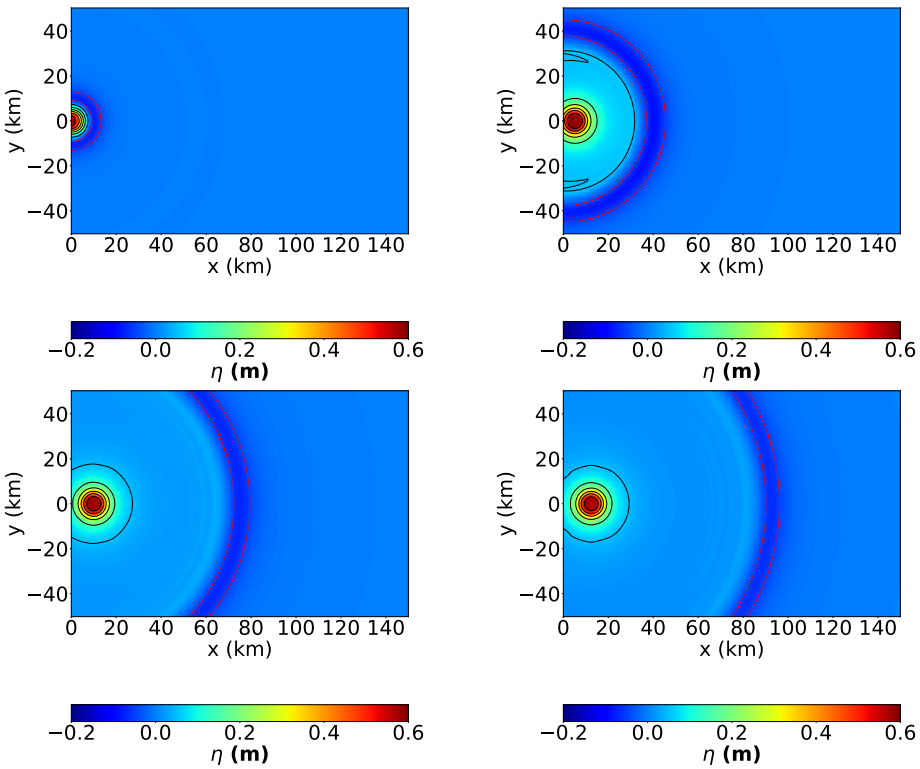

Figure 2.16. Free surface elevation induced by moving pressure field of duration 50, $V_x = 35$ km/h, $V_y = 0$ km/h seconds in cartesian reference frame for t = 100, 500, 1000, 1250 seconds

In all three cases, since the water elevation is substantially different, the linearity hypothesis would appear to be unconfirmed. This happens because, while reproducing a real cyclone path, which is a continuous phenomenon by discretizing it, the aliasing problem intervenes. Aliasing refers to the phenomenon where a signal that is sampled at too low rate in the time domain discrete intervals is misrepresented or distorted. So Δt that have been chosen for the comparison are too high causes so that aliasing problem verify.

To avoid this problem in reproducing the correct path of the cyclone's eye, the duration of the impulses used to discretize the cyclone's continuous source term should be low enough. Then, a Courant-like number (C) may be used:

$$C = V \frac{\Delta t}{R_{max}} < C_{max} \tag{2.40}$$

It should be noted that the parameter C is not influenced by the resolution of the regular grid the analytical solution is mapped on. Indeed, the

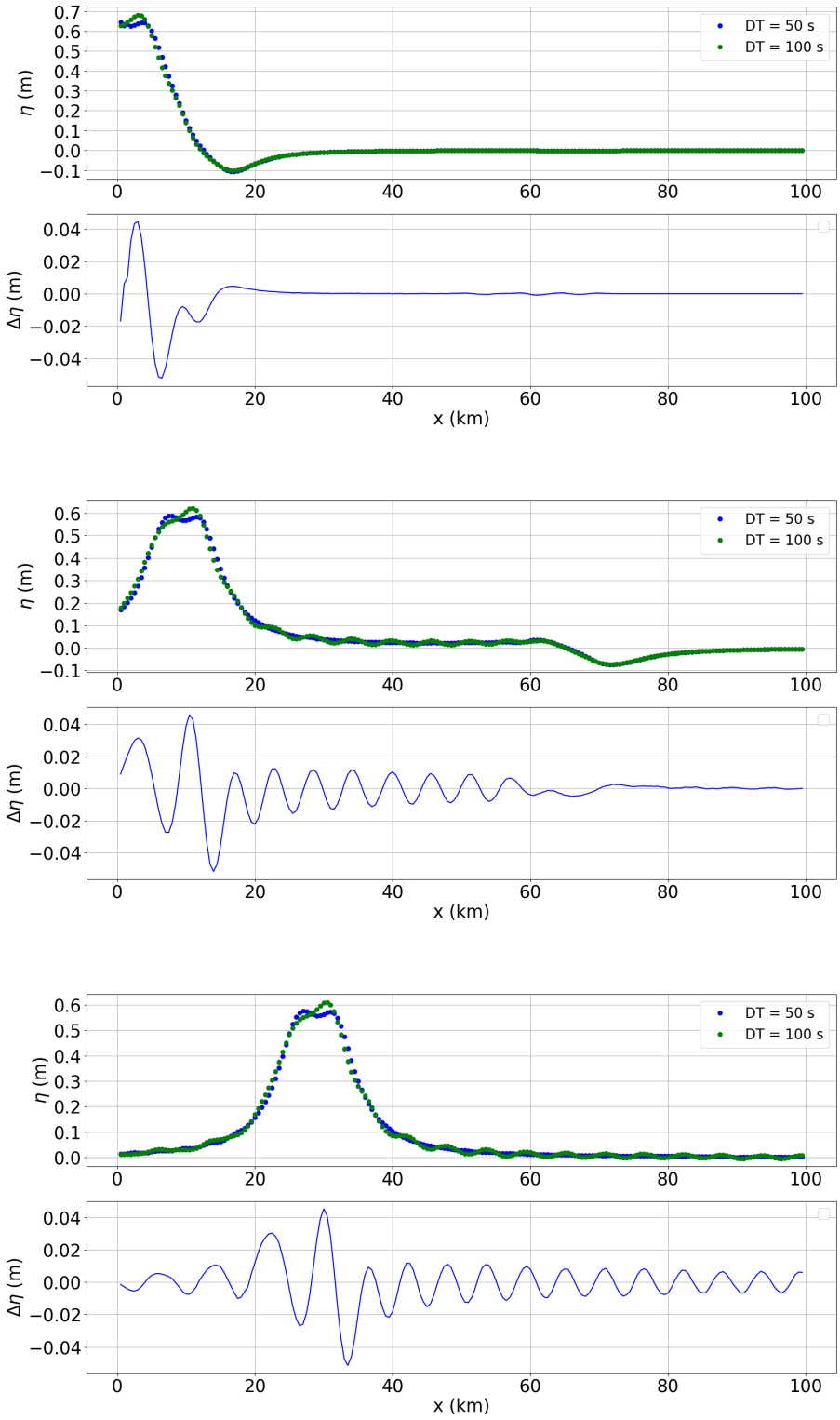

Figure 2.17. Comparison of the free surface elevation generated by moving pressure impulses of duration 50 s and 100 s for t = 200, 1000, 3000 s.

parameter is aimed to correctly discretize the cyclone's path in a series of impulses of a given temporal duration besides the location of the points

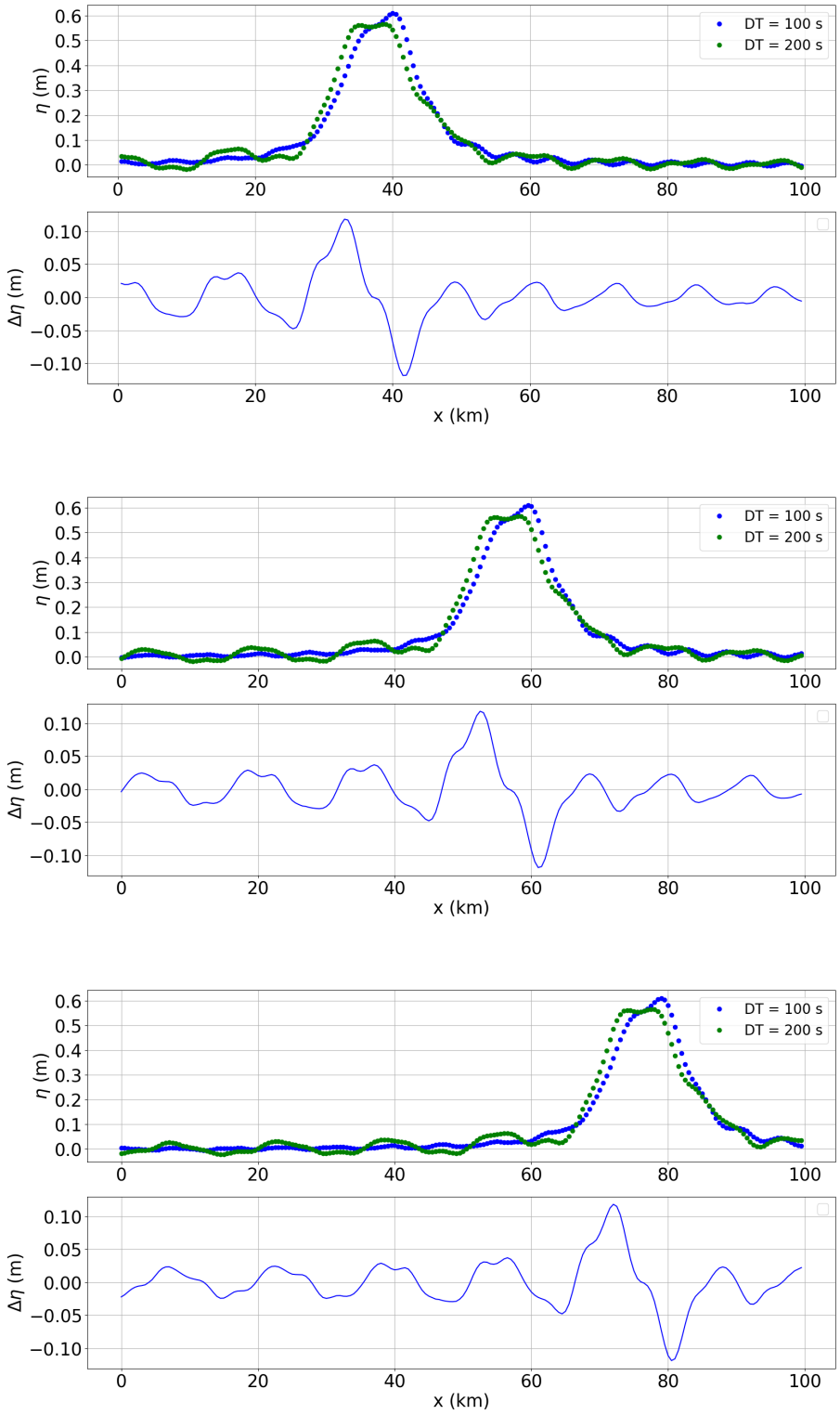

Figure 2.18. Comparison of the free surface elevation generated by moving pressure impulses of duration of 100 s and 200 s for t = 1000,1800,3600 seconds.

where the analytical solution is estimated.

A sensitivity analysis has been carried out and the value of C_{max} has

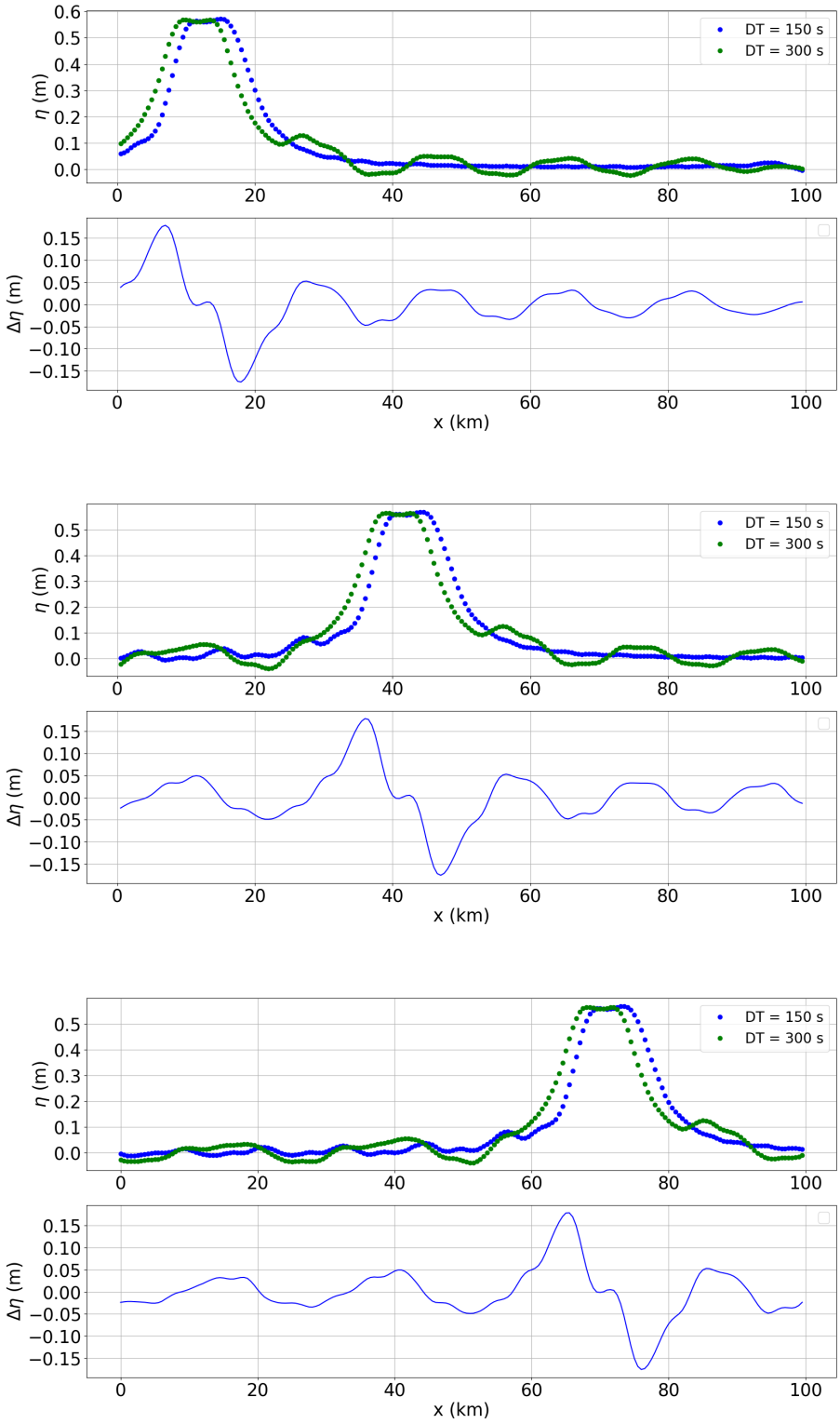

Figure 2.19. Comparison of the free surface elevation generated by moving pressure impulses of duration of 150 s and duration 300 s for t = 6000, 6900,12000 s.

been estimated as 0.015 so that $\Delta t_{max} = 25s$. As shown in figure 2.20 using moving cyclone discretized with $\Delta t = 25$ s allows to apply superposition of effect reproducing correctly free surface elevation evolution.

It must be stressed that while adopting a correct Δt to discretize the cyclone path, still introducing translation velocity to the pressure field, peak elevation still correctly reproduces the inverse baric effect as stated by Ponte et al. (1991).

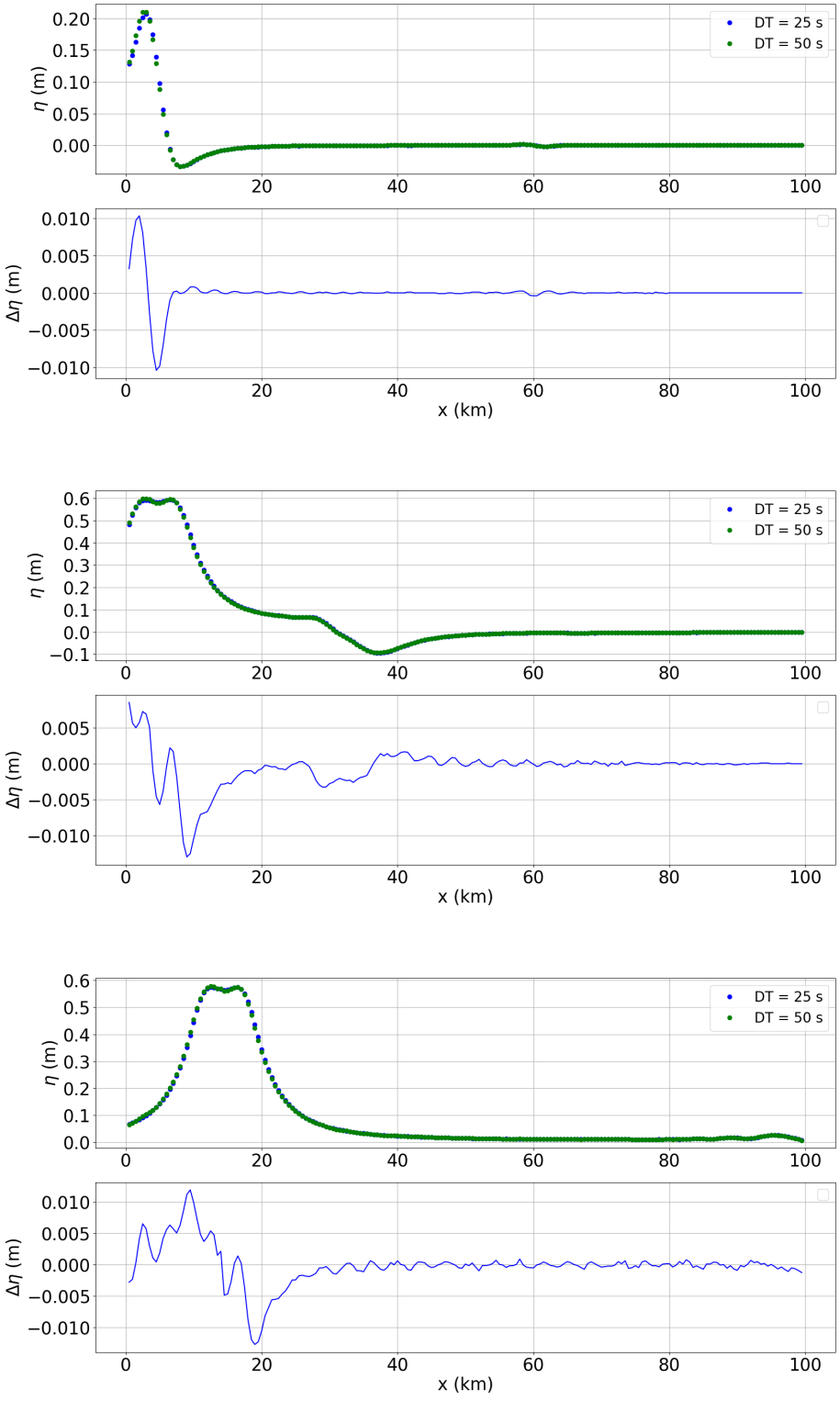

Figure 2.20. Snapshots of confrontation of the free surface elevation generated a cyclone discretized with $\Delta t = 25$ seconds and $\Delta t = 50$ for t = 25, 250 and 750 s

Numerical applications to ideal cases

Chapter abstract
In this chapter Delft3d-Flow model will be introduced. Equations and input files necessary to set up hydrodynamic simulations will be described. Then numerical model will be used to validate the proposed analytical model. In the end the numerical model will be forced by imposing the analytical boundary conditions.

3.1 The numerical model

The analytical model has been applied to define the analytical boundary conditions for a series of numerical experiments carried out by means of Delft3D-FLOW numerical model Deltares (2013). It simulates either two-dimensional (2DH, depth-averaged) or three-dimensional (3D) unsteady flows and transport phenomena resulting from tidal and/or meteorological forcing, including the effect of density gradients due to a non-uniform temperature and salinity distribution (density-driven flow). In general, Delft3D-FLOW solves the Navier-Stokes equations for incompressible fluids, under the Boussinesq assumptions in two (depth-averaged) or three dimensions. The system of governing equations consists of the horizontal momentum equations, the continuity equation, and the transport equations for conservative constituents.

The model has been used to solve the two-dimensional hydrodynamics induced by a moving pressure impulse. Then, governing equations, for orthogonal curvilinear coordinates, read as follow:

$$\frac{\delta\xi}{\delta t} + \frac{1}{\sqrt{G_{\xi\xi}}\sqrt{G_{\eta\eta}}}\frac{\delta(d+\xi)U\sqrt{G_{\eta\eta}}}{\delta\xi} + \frac{1}{\sqrt{G_{\xi\xi}}\sqrt{G_{\eta\eta}}}\frac{\delta(d+\xi)V\sqrt{G_{\xi\xi}}}{\delta\xi} = \\ = (d+\xi)Q \tag{3.1}$$

$$\frac{\partial u}{\partial t} + \frac{u}{\sqrt{G_{\xi\xi}}}\frac{\partial u}{\partial \xi} + \frac{v}{\sqrt{G_{\eta\eta}}}\frac{\partial u}{\partial \eta} + \frac{\omega}{d+\zeta}\frac{\partial u}{\partial \sigma} - \frac{v^2}{\sqrt{G_{\xi\xi}}\sqrt{G_{\eta\eta}}}\frac{\partial\sqrt{G_{\eta\eta}}}{\partial\xi} + \\ + \frac{uv}{\sqrt{G_{\xi\xi}}\sqrt{G_{\eta\eta}}}\frac{\partial\sqrt{G_{\xi\xi}}}{\partial\eta} - fv = -\frac{1}{\rho_0\sqrt{G_{\xi\xi}}}P_\xi + F_\xi + \\ + \frac{1}{(d+\zeta)^2}\frac{\partial}{\partial\sigma}\left(\nu_V\frac{\partial u}{\partial\sigma}\right) + M_\xi \tag{3.2}$$

$$\frac{\partial v}{\partial t} + \frac{u}{\sqrt{G_{\xi\xi}}}\frac{\partial v}{\partial \xi} + \frac{v}{\sqrt{G_{\eta\eta}}}\frac{\partial v}{\partial \eta} + \frac{\omega}{d+\zeta}\frac{\partial v}{\partial \sigma} - \frac{uv}{\sqrt{G_{\xi\xi}}\sqrt{G_{\eta\eta}}}\frac{\partial\sqrt{G_{\eta\eta}}}{\partial\xi} + \\ - \frac{u^2}{\sqrt{G_{\xi\xi}}\sqrt{G_{\eta\eta}}}\frac{\partial\sqrt{G_{\xi\xi}}}{\partial\eta} - fu = -\frac{1}{\rho_0\sqrt{G_{\xi\xi}}}P_\eta + F_\eta + \\ + \frac{1}{(d+\zeta)^2}\frac{\partial}{\partial\sigma}\left(\nu_V\frac{\partial v}{\partial\sigma}\right) + M_\eta \tag{3.3}$$

where ξ and η are the horizontal curvilinear coordinates, u, and v are the flow velocity components along the ξ- and η-direction respectively, $G_{\eta\eta}$ and $G_{\xi\xi}$ coefficients used to transform curvilinear to rectangular coordinates since, in the model, Cartesian reference frame is considered as a specific application of the curvilinear; σ is the vertical coordinate; d is the still water level, ζ is the free surface elevation (positive upward); f is the Coriolis parameter; P_ξ and P_η represent the pressure gradients; F_ξ and F_η in the momentum equations represent the unbalance of horizontal Reynold's stresses; ν_u and ν_v define eddy viscosity along ξ- and η-direction respectively; σ is the z coordinate; M_ξ and M_η represent the components along ξ- and η-direction respectively due to contributions related to external sources or sinks of momentum (external forces by hydraulic structures, discharge or withdrawal of water, wave stresses, etc.).

It has to be stressed that the cartesian (O, x, y) reference frame, used for the numerical simulation described in the following, is a particular case of the horizontal curvilinear coordinates.

The computational grid is a staggered Arakawa C grid so that, considering a square computational volume control, on the four vertex of water depth is defined, in the middle of lower and upper side the y-component of velocity is defined, in the middle of the left and right side the x-component of velocity is defined, while in the center water level and constituent are defined. Supposing to define a rectilinear grid in a channel of dimensions $L_x = 10000$ m $L_y = 5000$ m with a spatial resolution of 1000 m, this will require $nx = 11$ and $ny = 6$ grid points.

For this work, the free source code of Delft3D-flow, version 6.04.00.140218M has been compiled. The free version does come with the GUI so a python code has been realized to create all the necessary files to simulate various hydrodynamic scenarios.

3.2 Numerical model validation

The numerical model validation is performed by comparing results obtained from the analytical model itself and numerical simulation performed in the same conditions. First, different pressure fields have been considered. Five pressure fields have been chosen each one with $p_{drop} = 5500$ Pa. All the

Name	R (km)	p_{drop} (Pa)	A	B
Test1	100	5500	40	1.8
Test2	60	5500	40	2.2
Test3	40	5500	40	2.6
Test4	20	5500	40	3.0
Test5	100	5500	80	2.0

Table 3.1. Ideal cyclone definition

characteristics are reported in table 3.1.

The numerical grid has been realized as schematized in figure 3.1 where the grid is symmetric with respect of the y-axis and extends from -50 km to +50 km along it. The x-axis extends from 0 km to +120 km. The coordinates of the cyclone's eye at t = 0 s are x = -50 km and y = 0 km. The red line indicates the cyclone path while the green ones indicates the section for which results will be extracted and compared with the analytical ones. In particular, results will be obtained for all the y at section x = 30 km and for x values that go from 0 to 120 km for y = 0 km. Numerical grid resolution has been set to 500 m in both the x and y axes so that the result comparison could be performed on the same point and no interpolation process is needed. Bathymetry is considered constant and equal to 300 m. As for the analytical model, the pressure field is given every 25 seconds while the numerical time step has been set to 2.5 seconds.

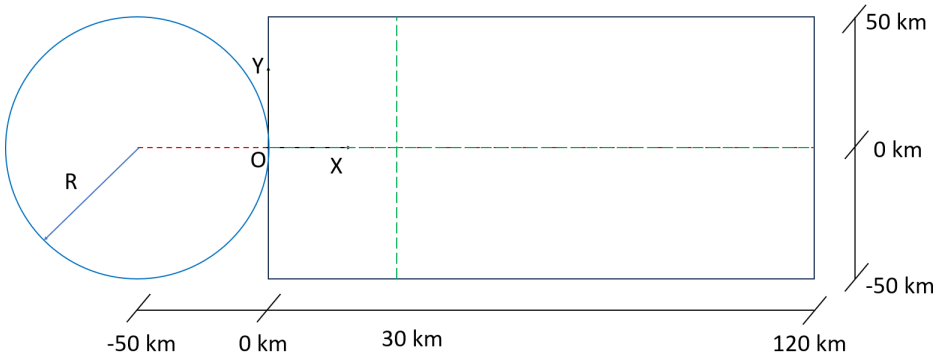

Figure 3.1. Numerical grid realised for the validation process.

Results performed with numerical simulations are influenced by boundary conditions, so they must be applied correctly to obtain comparable results. Riemann conditions have been applied to all four boundaries so that water oscillations are allowed to radiate inside of the computational

grid. For every test case three snapshots along the y = 0 km section and three for the x = 30 km, at the same time instant, will be reported in figures 3.2, 3.3, and figures C.1, C.2, C.3, C.4,C.5, C.6, C.7 and C.8 reported in appendix B.

Starting considering the x = 30 km section, it can be said that the analytical and numerical model comparison is satisfactory from a qualitative point of view. For Test1 difference between the to patterns is in the order of the centimeter. In the early stages of simulation, the analytical model gives a higher surface level than the numerical one, especially for y section especially for sections from y = 20 km while for later stages, the analytical difference became almost constant. The same verifies for Test2, Test3, Test4 and Test5. It can also be observed that the higher superposition of the two calculated surface levels is obtained for cyclone radius R decreases. This happens since numerical results are highly influenced by boundary conditions. For cyclones with a radius fully contained inside the numerical domain, the boundary effect becomes less relevant so analytical and numerical results tend to equate. The same can be observed by analyzing results for y =0 km. For Test1 and Test5, both performed considering a cyclone radius of 100 km, for t = 115 minutes differences between the approaches became higher for higher x coordinate values since the pressure field that induced the free surface elevation is still not fully contained in the computational domain. For Test2, Test3, and Test4 since the radii are respectively 60, 40, and 20 km, for the considered time frame, the boundary effect has a reduced effect, so the difference between analytical and numerical results tends to zero. However, the proposed analytical model, being set with the right parameters as described in Chapter 2, is highly reliable since the induced water level propagates at the same celerity, and the plateau water surface induced by the cyclone's eye pressure value is well reproduced. Also, the analytical model gives results that are independent of the computational grid, with the same spatial and temporal resolution.

3.3 Numerical application

Since analytical and numerical comparisons have been characterized by reasonable results, numerical simulations have been implemented to use

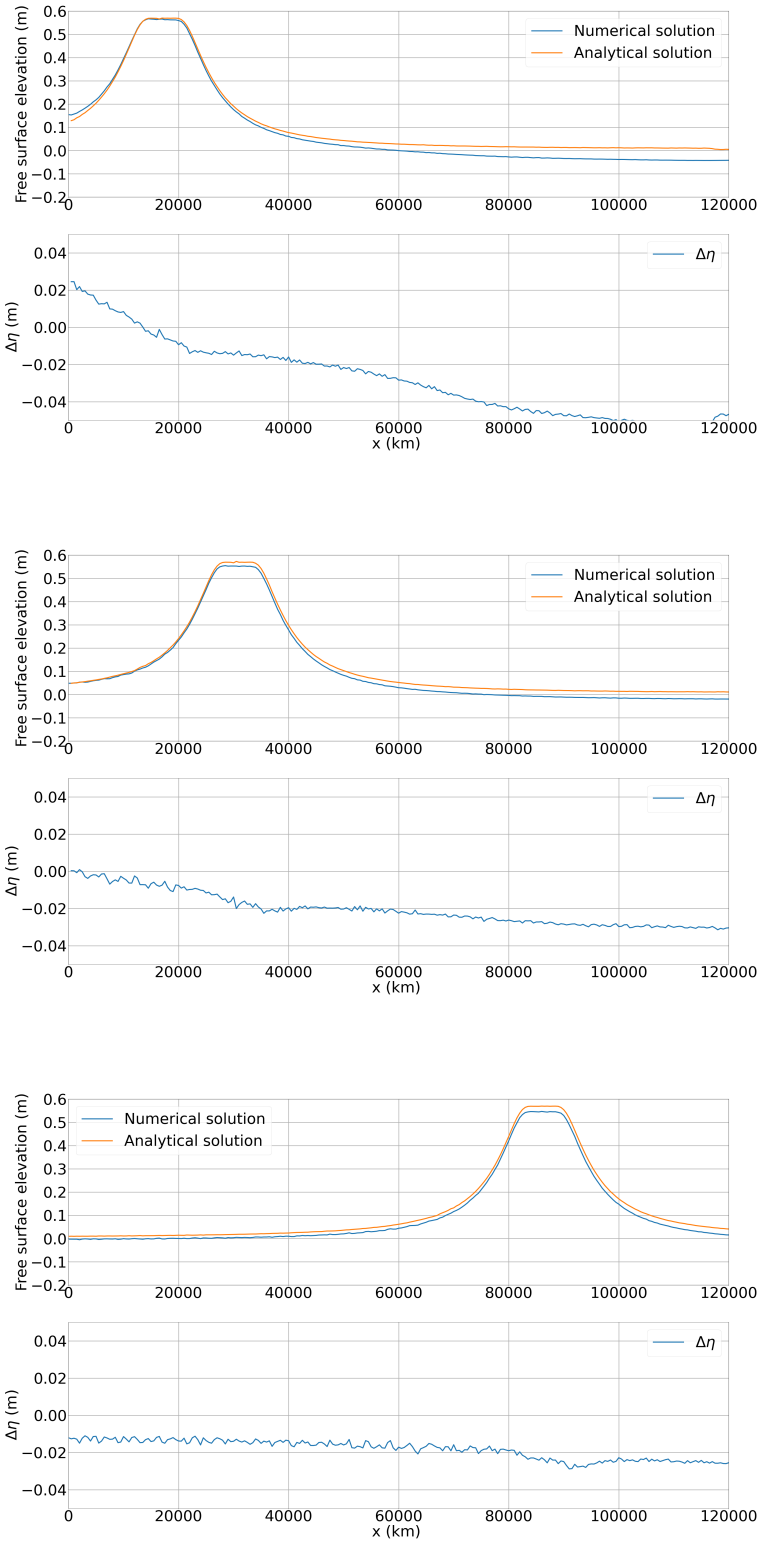

Figure 3.2. Test1 result obtained for y = 0 km for t = 115, 138.3 and 235 minutes

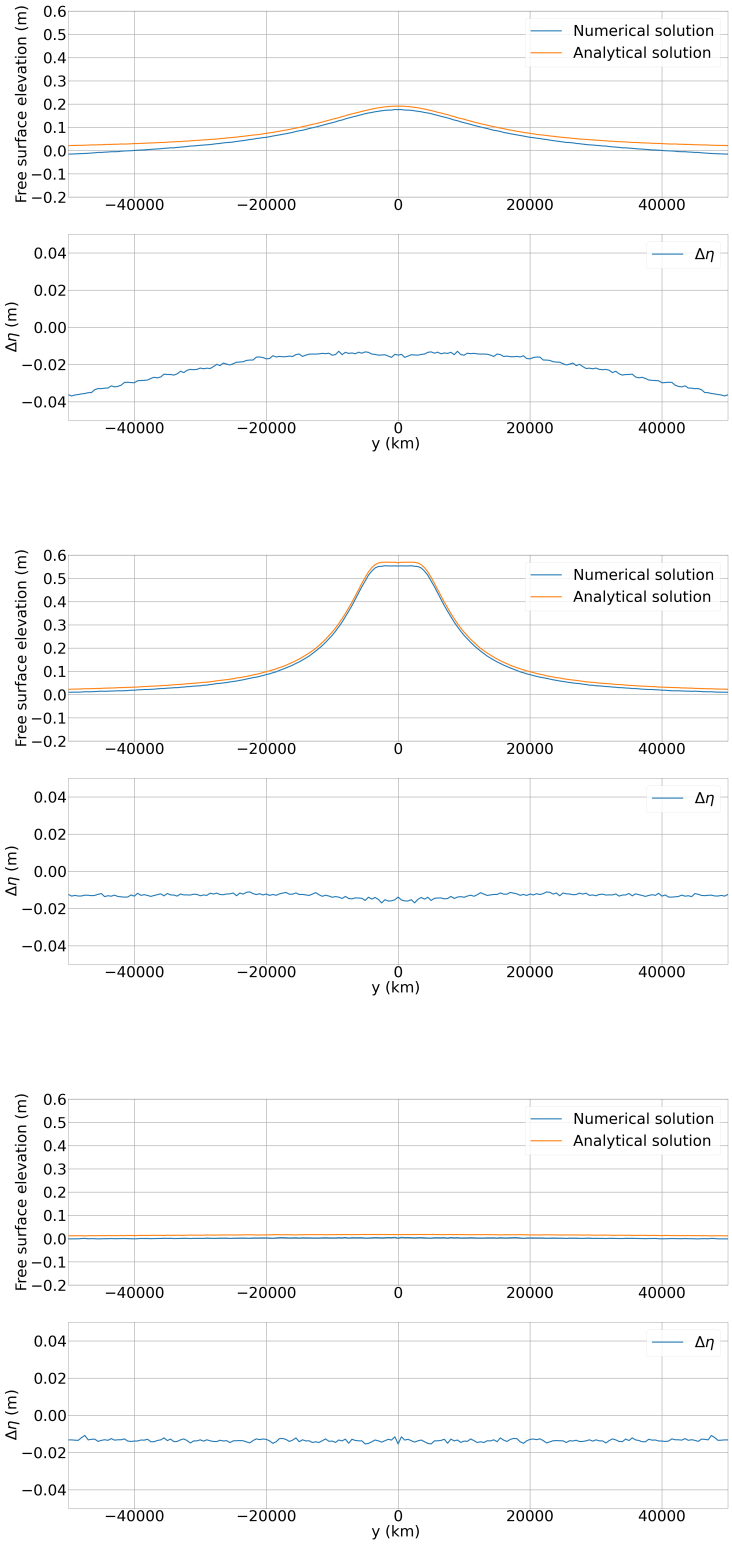

Figure 3.3. Test1 result obtained for x = 30 km for t = 115, 138.3 and 235 minutes

analytical boundary conditions. Numerical simulations can be divided into two categories. The first aim to describe how adopting analytical boundary conditions and reducing numerical grid extension while leaving unaltered space resolution influences results and simulation time. The second one aims to compare water elevation time series for a specific point using a coarse grid and a fine grid with a higher spatial resolution.

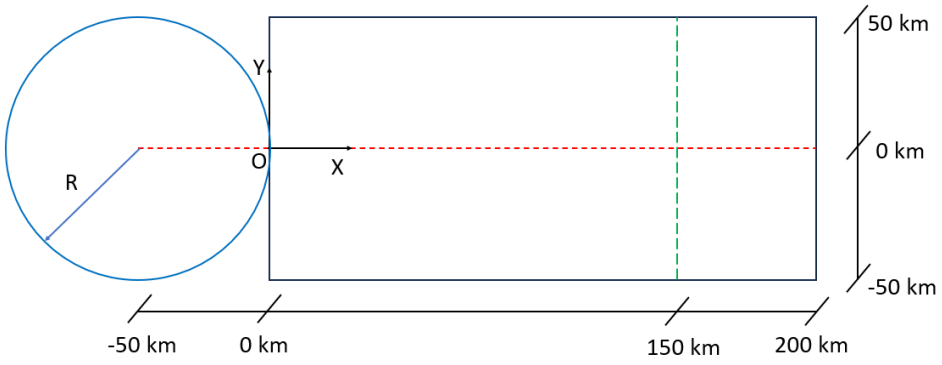

Figure 3.4. Numerical grid configuration used to apply analytical boundary conditions and to reduce grid extension

Referring to figure 3.4, the coarse grid extends along the x-axis for 200 km and along the y-axis for 100 km. Spatial resolution is the same for the x and y axis and is set to 250 m. On the other hand fine grid extends along the x-axis for 50 km and along the y-axis for 100 km. With respect of the coarse grid, the fine has the origin in x=150 km and y=0. The analytical boundary conditions were applied precisely at x=150 km. The simulation covers the action of a hurricane with p_{drop} = 5500 Pa, $A = 40\ km^B$ and B = 1.8 (-) (i.e Test1) with the cyclone's eye at x= -50 km and y = 0 km at t=0 s and moving with V_x = 35 km/h and V_y = 0 km/h. The hurricane action lasted for 10 hours, and it has been discretized with a Δt = 25 s, while the numerical time step has been set to 2.5 s.

As shown in the snapshot in 3.5 the water elevation obtained with an analytical-numerical not only gives higher elevation but also, this new mixed approach allowed to change the simulation running time from the 40 minutes of the coarse to the 8 minutes of the fine grid.

Instead, if the focus is on a specific point of interest, it should be stressed that the computational domain must be large enough to prevent the boundary conditions from affecting the result itself. Because of that it could be problematic to obtain correct results for point of interest that lies near the

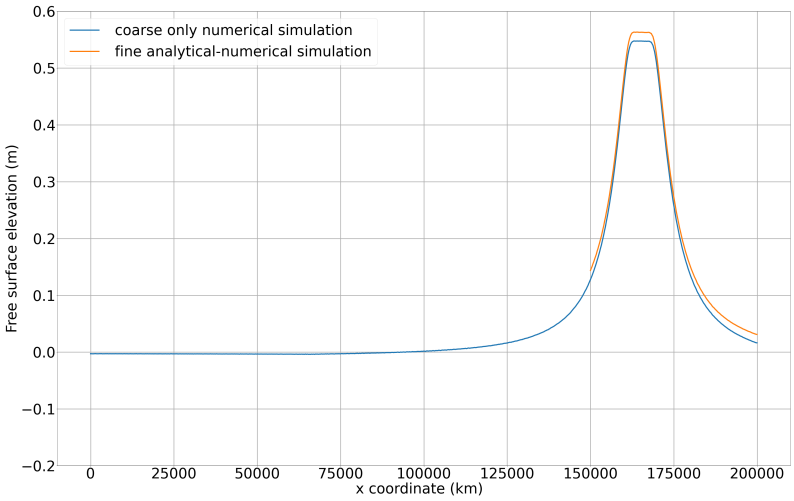

Figure 3.5. Comparison of the water elevation computed by a coarse and only numerical simulation and a fine simulation where analytical boundary conditions have been applied.

computational boundary. So the analytical model has been applied as it follows.

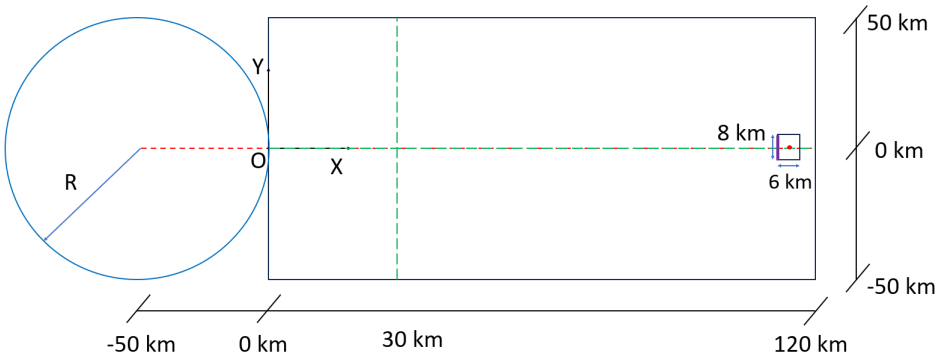

Figure 3.6. Numerical grid realised for the validation process.

Referring figure 3.6, the same numerical simulation, for the same cyclone configuration has been considered. Then a smaller grid configuration has been reproduced. The new grid extends for 6 km along the x-axis and for 8 km along the y-axis. Its origin, with respect to the largest grid origin, is x = 110 km and y = 0. Its spatial resolution is $dx = dy = 50$ m. On its left boundary, plotted in violet, analytical boundary conditions are imposed while on the other boundary Riemann conditions are imposed. This new smaller grid configuration is referred to as fine configuration while the one used previously as coarse simulation. Free surface evolution has

been extracted for the point (plotted in red) x = 115 km and y =0 km, for both configurations.

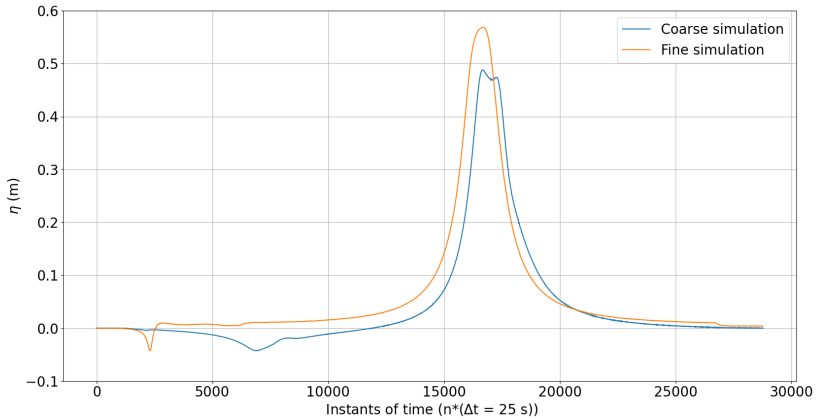

Figure 3.7. Confrontation of temporal series for point x = 115 km and y = 0 km performed with Test1 cyclone pressure field.

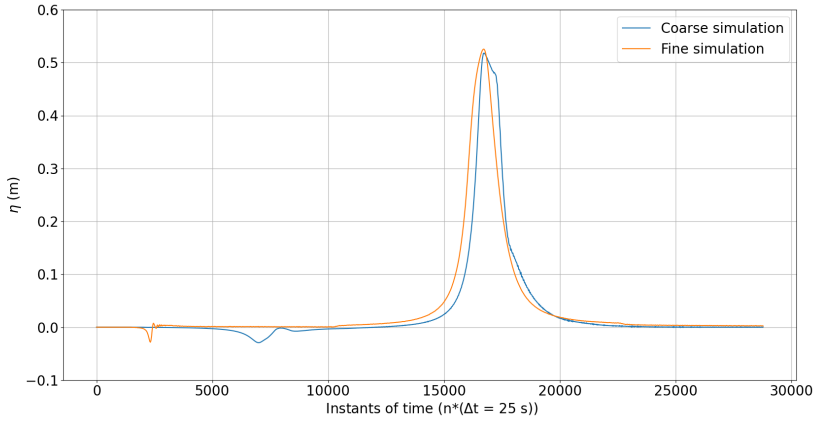

Figure 3.8. Confrontation of temporal series for point x = 115 km and y = 0 km performed with Test2 cyclone pressure field.

It has to be stressed that since cyclone pressure field needs a computational grid that extends for a length comparable with its radius, fine grid simulations are performed without imposing any pressure field. Comparison for all cyclone configurations induced free surface elevation are reported in figure 3.7, 3.8, 3.9, 3.10 and 3.12.

To better understand the significance of the results, we first focus on the numerical time series. Considering the time series for y=0 km realized in order to validate the analytical model and therefore realized with a large-scale computational grid, and reported in the previous section, it

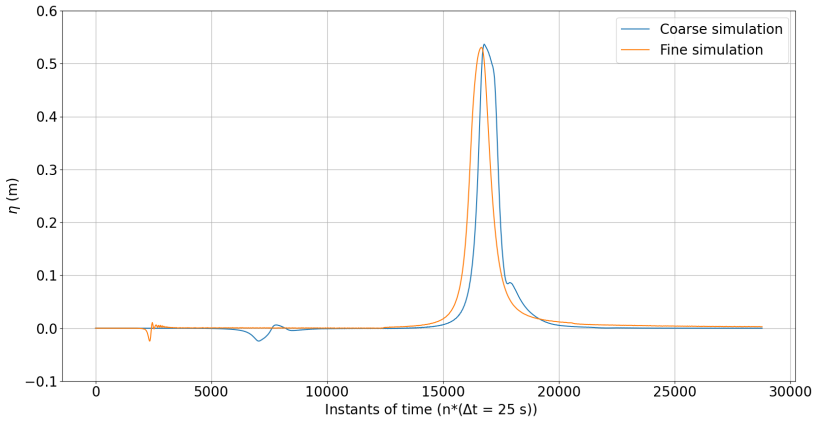

Figure 3.9. Confrontation of temporal series for point x = 115 km and y = 0 km performed with Test3 cyclone pressure field.

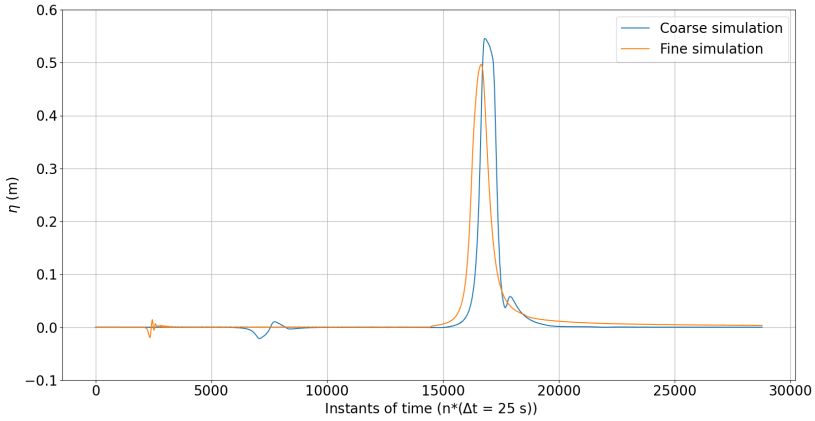

Figure 3.10. Confrontation of temporal series for point x = 115 km and y = 0 km performed with Test4 cyclone pressure field.

appears that the maximum elevation induced by all the cyclonic configurations considered (table) is about 0.55 m. Since pdrop = 5500 Pa, the results confirm the theoretical results obtainable by applying the inverse baric effect. Extracting the results from the same simulations for the point of interest, it can be seen that for Test1 the peak level becomes about 48 cm, for Test2 about 52 cm, for Test3 almost 54 cm, for Test4 54.5 cm and for Test5 about 48 cm. The greatest decreases in peak heights occur for the Test1, Test2 and partly Test3 configurations. The three configurations are characterized by cyclones with a radius of 100, 100, and 60 km, so the decrease in levels can be attributed to edge effects. In fact, since the point of interest is near the right-hand boundary of the computational domain,

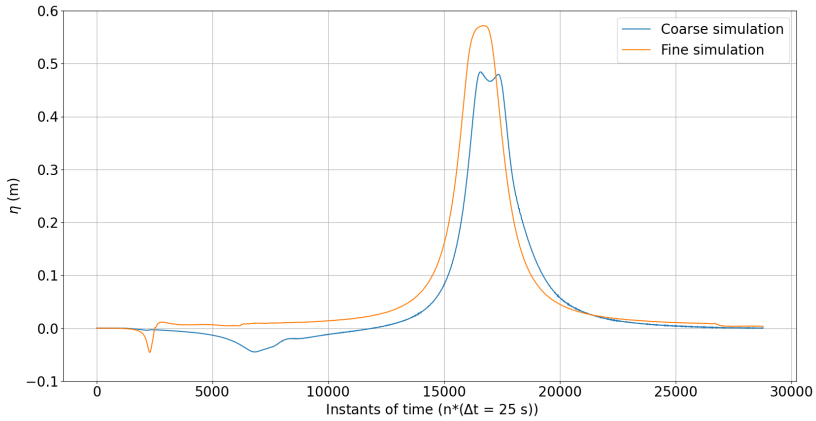

Figure 3.11. Confrontation of temporal series for point x = 115 km and y = 0 km performed with Test5 cyclone pressure field.

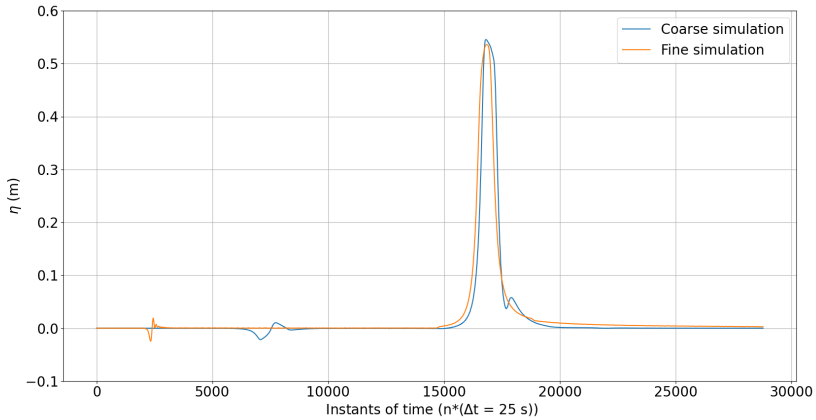

Figure 3.12. Confrontation of temporal series for point x = 115 km and y = 0 km performed with Test5 cyclone pressure field obtained for fine grid wth x origin at 113 km.

part of the pressure field inducing the level increase is already outside the domain itself. It is therefore possible to say that the free surface elevation does not develop completely. On the contrary for Test3 and Test4, the cyclones considered have a radius of 40 and 20 km and therefore the edge effects are less appreciable although they are present. Considering now the results obtained using a small-scale configuration in which the analytical boundary conditions have been imposed, it is possible to observe a different trend. For Test1 the peak is unchanged, as well as for Test5, for Test2 and Test3 it is about 53 cm while for Test4 the level is lowered up to 49.5 cm. Although these results appear to be counterintuitive, the reasons for this

trend can be attributed to the boundary conditions themselves. In fact, for the configurations Test1, Test2 and Test5, the fact the cyclones considered induce a plateau in free surface elevation that once applied as a condition to the boundary, The evolution of the water level is spread within the computational grid, keeping the peak value almost unchanged. For Test3 and Test4 the plateau is smaller and therefore the numerical simulation results indicate a reduction of the peak value of the water level for points distant from the boundary where the analytical time series are imposed. As proof of this, if we consider a simulation with a reduced grid that, however, extends for 3 km with the x-axis originating in X = 113 km compared to the wide grid configuration, the results obtained are significantly different, with a peak of 53.5 cm. Also, the fact that fine simulations are only forced by boundary conditions explains why temporal series are not perfectly in phase but the fine ones tend to anticipate the growth phase.

Results show that, not only the analytical model itself but also its application produces highly reliable results. Still grid effect remains, opposite the only numerical approach. The model application describes with a good fit free surface elevation induced by cyclones with extended pressure ranges for specific points of interest. While the pressure field range decreases so must done with the distance between boundary side on which boundary conditions will be applied and the point of interest itself. It must also be said that fine numerical simulation requires almost 30% less simulation time.

Concluding remarks

A novel analytical approach to study water motion induced by cyclone pressure field is derived. The model relies on the theory of linear systems. Doing so free surface elevation can be formulated as a response function of the cyclone pressure field. Later, the actual path of the cyclone and its effect can be obtained by applying the superposition of effect. The model is derived following Le Mehaute approach [Le Méhauté and Wang (1996)] so that an instantaneous response function to a generic pressure field is first formulated and then the actual response function is obtained by applying the convolution integral. The instantaneous response function is obtained by considering linear and irrotational flow so that a potential wave function can be formulated to get, by using opportune boundary condition the free surface elevation η(r,t). The procedure is based on an adimensional approach and a cylindrical coordinate system so that the potential function is obtained by resolving the Laplace equation using the variable separation method. To consider an actual cyclone pressure field the Holland [Holland (1980)] parametric wind-pressure model is used. Since wind waves have not been considered, the only pressure contribution is taken into account. Pressure definition is given by (2.27) where p_{drop} is the difference between the undisturbed atmospheric pressure and cyclone's eye pressure. A and B are two scale parameters; A describes the radius of maximum wind location, hence the cyclone's eye extension; B determines how much the pressure drop occurs near the cyclone's eye.

The Holland pressure definition allows to write first the forcing term $H_I(k)$, equation (2.29), and so the impulse response function $\eta_U(r,t)$ is

obtained (eq. 2.30).

To achieve analytical results sensitivity analysis has been performed. Multiple ideal cyclones have been applied so that, for each one, using equation 2.27, the radius has been calculated. Doing so upper integral limit has been determined so that equation 2.29 can be used to determine, for each case, the value of k_{max} with k being the wave number. Also, sensitivity analysis has been performed to determine the resolution of k vector, dk. Then, choosing a single pressure field, free surface elevation evolution has been studied for an instantaneous impulse, and multiple finite duration impulses fixed in space. Model performance has been evaluated by confronting free surface elevation induced by different durations. In this case error in the order of 10^{-5} m have been obtained and are due to numerical approximations. Also moving pressure field are considered so that actual effect of cyclone are studied. First, two coordinate transformations have been performed in order to have a global cartesian space in which the cyclone's pressure field could move. While introducing translation velocity, aliasing problems emerge so that a Courant-like number has been introduced in order to determine a correct temporal resolution. Then, validation processes have been performed. It consists of comparing analytical and numerical results obtained for the same cyclone positioning, forward speed, temporal and spatial resolution. Results have been extracted for specific y and x sections. Confronting result emerges that analytical model reproduces with high-reliability free surface elevation in both peak elevation and extension. For these reasons, the proposed analytical model has been applied to describe reliable boundary conditions in terms of water elevation time series so that detailed simulation can be performed. Then numerical simulations have been performed to include the analytical boundary conditions. First, two numerical scenarios have been considered, one in which only numerical model has been used, and another where numerical and analytical boundary conditions have been applied. The two grid have the same spatial resolution and both extend from -50 km to 50 km on the y-axis. On the other hand the first extend for 200 km while the second for only 50 km. Results, of which a snapshot is reported in figure 3.5 show that the analytical-numerical approach induces higher water elevation val-

ues then the results are in favor of safety. Also it could be observed that time simulation decrease of 32 minutes.

On the other hand, if the focus is on a specific point of interest, the process consists of confronting numerical results produced for all cyclone configurations adopting a large computational domain with a smaller grid configuration in which analytical boundary conditions are applied. Results are then confronted for a specific point of interest. It emerges that while purely numerical simulation are influenced by boundary conditions so that time series extracted for point near the boundary shows how level induced by the pressure are lower than the theoretical one since the pressure field itself starts go exit from the computational grid, the proposed applications is highly influenced by the plateau of free surface elevation. This is due to the fact that elevations of the free surface with reduced plateau, which are generated by cyclones with smaller radii, tend to propagate in the calculation grid reducing the peak height. It appears clear the many advantages that derive from applying this new novel approach. On one side, time simulation can be highly reduced by applying analytical boundary conditions while not reducing y-axis extension so that results can be analyzed for multiple points. On the other hand, if only few points are objects of analysis, analytical boundary conditions can be applied to perform simulations implementing numerical grid with spatial resolution in the order of 50 m.

Bibliography

Alfieri, L., Salamon, P., Pappenberger, F., Wetterhall, F., and Thielen, J. (2012). Operational early warning systems for water-related hazards in europe. *Environmental Science & Policy*, 21:35–49.

Bhaskaran, P. K., Gayathri, R., Murty, P., Bonthu, S., and Sen, D. (2014). A numerical study of coastal inundation and its validation for thane cyclone in the bay of bengal. *Coastal Engineering*, 83:108–118.

Cavicchia, L., von Storch, H., and Gualdi, S. (2014). A long-term climatology of medicanes. *Climate dynamics*, 43:1183–1195.

Chan, J. C. (2005). The physics of tropical cyclone motion. *Annu. Rev. Fluid Mech.*, 37:99–128.

Decker, M., Brunke, M. A., Wang, Z., Sakaguchi, K., Zeng, X., and Bosilovich, M. G. (2012). Evaluation of the reanalysis products from gsfc, ncep, and ecmwf using flux tower observations. *Journal of Climate*, 25(6):1916–1944.

Deltares, D. (2013). Delft3d-flow user manual. *Deltares Delft, The Netherlands*, 330.

Di Risio, M., Pasquali, D., Lisi, I., Romano, A., Gabellini, M., and De Girolamo, P. (2017). An analytical model for preliminary assessment of dredging-induced sediment plume of far-field evolution for spatial non homogeneous and time varying resuspension sources. *Coastal Engineering*, 127:106–118.

Elsner, J. B. (2020). Continued increases in the intensity of strong tropical cyclones. *Bulletin of the American Meteorological Society*, 101(8):E1301–E1303.

Esteban, M., Takagi, H., and Thao, N. D. (2014). Tropical cyclone damage to coastal defenses: future influence of climate change and sea level rise on shallow coastal areas in southern vietnam. In *Coastal Disasters and Climate Change in Vietnam*, pages 233–255. Elsevier.

Holland, G. J. (1980). An analytic model of the wind and pressure profiles in hurricanes.

Hope, M. E., Westerink, J. J., Kennedy, A. B., Kerr, P., Dietrich, J. C., Dawson, C., Bender, C. J., Smith, J., Jensen, R. E., Zijlema, M., et al. (2013). Hindcast and validation of hurricane ike (2008) waves, forerunner, and storm surge. *Journal of Geophysical Research: Oceans*, 118(9):4424–4460.

Irish, J. L., Resio, D. T., and Ratcliff, J. J. (2008). The influence of storm size on hurricane surge. *Journal of Physical Oceanography*, 38(9):2003–2013.

Kalman, R. E. (1963). Mathematical description of linear dynamical systems. *Journal of the Society for Industrial and Applied Mathematics, Series A: Control*, 1(2):152–192.

Lagasio, M., Fagugli, G., Ferraris, L., Fiori, E., Gabellani, S., Masi, R., Mazzarella, V., Milelli, M., Parodi, A., Pignone, F., et al. (2022). A complete meteo-hydrological chain to support early warning systems from weather scenarios to flooded areas: the apollo medicane use case. In *EGU General Assembly Conference Abstracts*, pages EGU22–2622.

Le Méhauté, B. and Wang, S. (1996). *Water waves generated by underwater explosion*, volume 10. World Scientific.

McInnes, K., Walsh, K., Hubbert, G., and Beer, T. (2003). Impact of sea-level rise and storm surges on a coastal community. *Natural Hazards*, 30:187–207.

Montgomery, M. T. and Farrell, B. F. (1993). Tropical cyclone formation. *Journal of Atmospheric Sciences*, 50(2):285–310.

Mylonas, M. P., Douvis, K. C., Polychroni, I. D., Politi, N., and Nastos, P. T. (2019). Analysis of a mediterranean tropical-like cyclone. sensi-

tivity to wrf parameterizations and horizontal resolution. *Atmosphere*, 10(8):425.

Pasquali, D., Bruno, M., Celli, D., Damiani, L., and Di Risio, M. (2019). A simplified hindcast method for the estimation of extreme storm surge events in semi-enclosed basins. *Applied Ocean Research*, 85:45–52.

Ponte, R. M., Salstein, D. A., and Rosen, R. D. (1991). Sea level response to pressure forcing in a barotropic numerical model. *Journal of physical oceanography*, 21(7):1043–1057.

Proudman, J. (1929). The effects on the sea of changes in atmospheric pressure. *Geophysical Supplements to the Monthly Notices of the Royal Astronomical Society*, 2(4):197–209.

Quader, M. A., Khan, A. U., and Kervyn, M. (2017). Assessing risks from cyclones for human lives and livelihoods in the coastal region of bangladesh. *International journal of environmental research and public health*, 14(8):831.

Rego, J. L. and Li, C. (2009). On the importance of the forward speed of hurricanes in storm surge forecasting: A numerical study. *Geophysical Research Letters*, 36(7).

Smith, R. K., Schmidt, C. W., and Montgomery, M. T. (2011). An investigation of rotational influences on tropical-cyclone size and intensity. *Quarterly Journal of the Royal Meteorological Society*, 137(660):1841–1855.

Taylor, H. T., Ward, B., Willis, M., and Zaleski, W. (2010). The saffir-simpson hurricane wind scale. *Atmospheric Administration: Washington, DC, USA*.

Tory, K. J. and Frank, W. M. (2010). Tropical cyclone formation. *Global perspectives on tropical cyclones: From science to mitigation*, pages 55–91.

Tous, M. and Romero, R. (2013). Meteorological environments associated with medicane development. *International Journal of Climatology*, 33(1):1–14.

van Ormondt, M., van Dongeren, A., and Roelvink, D. (2021). A semi-empirical method for computing storm surges on open coasts during tropical cyclones. *Coastal Engineering*, 165:103839.

WaNg, Y. (2012). Recent research progress on tropical cyclone structure and intensity. *Tropical Cyclone Research and Review*, 1(2):254–275.

Westerink, J. J., Luettich, R. A., Feyen, J. C., Atkinson, J. H., Dawson, C., Roberts, H. J., Powell, M. D., Dunion, J. P., Kubatko, E. J., and Pourtaheri, H. (2008). A basin-to channel-scale unstructured grid hurricane storm surge model applied to southern louisiana. *Monthly weather review*, 136(3):833–864.

Zekkos, D., Zalachoris, G., Alvertos, A. E., Amatya, P. M., Stanley, T., et al. (2020). The september 18-20 2020 medicane ianos impact on greece phase i reconnaissance report. *UMBC GESTAR II Collection*.

Description of Delft3d-Flow file

To set up a hydrodynamic model input file must be prepared.

The Master Definition file (MDF file) is the input file for the hydrodynamic simulation program. It contains all the necessary data required for defining a model and running the simulation program as attribute files in which relevant data is stored such as xy grid, bathymetry, boundary and initial conditions and wind-pressure field, and physical parameters are set.

The orthogonal curvilinear xy grid file can be specified in the .grd file. This file contains a record where the Co-ordinate System is specified (Cartesian or Spherical) and a record with the missing value.

Also, the grid file will contain 2 blocks of ny rows, where ny is the number of points along the y-axis, with nx grid values, where nx is the number of points along the x-axis. The first block defines the x-coordinates while the second the y-coordinates.

Referring to the previous example the grid will be defined by $11x6$ points.

The computational grid enclosure is defined in the .enc file.

It contains the indices of the external computational grid enclosure so that every point is identified by one pair of M and N indices representing the grid coordinates where a line segment of the computational grid enclosure (polygon) changes direction. Referring to the previous example enclosure file will contain the points indices $(1, 1)$, $(12, 1)$, $(12, 7)$, and $(1, 7)$.

Also, bathymetry must be provided. In .dep file, depth values per row, starting at $N = 1$ to $N = nmax$, separated by one or more blanks, have to be given.

The open boundaries location can be indicated in .bnd file. For every label reported, the name of the open boundary section (max 20 characters), the type of boundary applied (1 character), and the type of data (1 character).

Boundary type can be:

- Z for water level conditions;
- C for current conditions;
- N for Neumann conditions;
- Q for discharge per grid cell conditions;
- T for total discharge for boundary section;
- R for Riemann conditions.

Data values can be defined as:

- A for astronomic component;
- H for harmonic flow boundary condition;
- Q when discharge (Q) and water height (H) tables are defined (only for water level boundaries);
- T when time-series is defined.

The open boundary section is individuated by point indices of the beginning and end points so that integers must be typed. Also, a reflection coefficient for short waves can be indicated but not for Neumann or Riemann conditions.

Each type of boundary condition corresponds to a file in which its values are reported.

For time series boundary conditions a .btc file must be realized which is provided for each open boundary segment with boundary data of type T (time series) the data in two related blocks as:

- a header block containing a number of keywords and their values are reported (as Boundary Section name, time unit, parameter, and unit);
- a data block containing the time series data.

Time series for space-varying wind velocity components and atmospheric pressure can be specified in the .wnd file. The file consists of a header, followed by data blocks containing the wind and pressure fields at times. In the header quantity as x-wind, y-wind and atmospheric pressure are defined as their unit and the time definition string must be stated with a fixed time string in which is mentioned the Δt passed since the reference date (indicated in the MDF file).

Examples of Delft3D-Flow files

In this appendix examples of Delft3D-Flow files are reported

```
300.000 300.000 300.000 300.000 300.000 300.000 300.000 300.000 300.000
300.000
300.000
300.000 300.000 300.000 300.000 300.000 300.000 300.000 300.000 300.000
300.000
300.000
300.000 300.000 300.000 300.000 300.000 300.000 300.000 300.000 300.000
300.000
300.000
300.000 300.000 300.000 300.000 300.000 300.000 300.000 300.000 300.000
300.000
300.000
300.000 300.000 300.000 300.000 300.000 300.000 300.000 300.000 300.000
300.000
300.000
300.000 300.000 300.000 300.000 300.000 300.000 300.000 300.000 300.000
300.000
300.000
```

Figure B.1. Example of .dep file.

```
Coordinate System = Cartesian
Missing Value     =    -9999
      10       5
 -999 -999 -999
ETA=    1       -0.0    1000.0    2000.0    3000.0
4000.0    5000.0    6000.0    7000.0    8000.0    9000.0
ETA=    2       -0.0    1000.0    2000.0    3000.0
4000.0    5000.0    6000.0    7000.0    8000.0    9000.0
ETA=    3       -0.0    1000.0    2000.0    3000.0
4000.0    5000.0    6000.0    7000.0    8000.0    9000.0
ETA=    4       -0.0    1000.0    2000.0    3000.0
4000.0    5000.0    6000.0    7000.0    8000.0    9000.0
ETA=    5       -0.0    1000.0    2000.0    3000.0
4000.0    5000.0    6000.0    7000.0    8000.0    9000.0
ETA=    1        0.0       0.0       0.0       0.0
0.0       0.0       0.0       0.0       0.0       0.0
ETA=    2     1000.0    1000.0    1000.0    1000.0
1000.0    1000.0    1000.0    1000.0    1000.0    1000.0
ETA=    3     2000.0    2000.0    2000.0    2000.0
2000.0    2000.0    2000.0    2000.0    2000.0    2000.0
ETA=    4     3000.0    3000.0    3000.0    3000.0
3000.0    3000.0    3000.0    3000.0    3000.0    3000.0
ETA=    5     4000.0    4000.0    4000.0    4000.0
4000.0    4000.0    4000.0    4000.0    4000.0    4000.0
```

Figure B.2. Example of .grd file.

```
1 1
11 1
11 6
1 6
1 1
```

Figure B.3. Example of .enc file.

```
SEABOUNDARY001       R T        1        2        1        3
1.0 Uniform
SEABOUNDARY002       R T        1        3        1        4
1.0 Uniform
SEABOUNDARY003       R T        1        4        1        5
1.0 Uniform
SEABOUNDARY004       R T        2        1       10        1
1.0 Uniform
SEABOUNDARY005       R T        2        6       10        6
1.0 Uniform
SEABOUNDARY006       R T       11        2       11        5
1.0 Uniform
```

Figure B.4. Example of .bnd file.

```
table-name           'Boundary Section : 1'
contents             'Uniform              '
location             'SEABOUNDARY001       '
time-function        'non-equidistant      '
reference-time       20200805
time-unit            'seconds'
interpolation        'linear'
parameter            'time' unit '[s]'
parameter            'Riemann         (R)  end A   uniform'     unit '[m]'
parameter            'Riemann         (R)  end B   uniform'     unit '[m]'
records-in-table     74
       0.00     0.000000     0.000000
      50.00     0.000000     0.000000
     100.00     0.000000     0.000000
     150.00     0.000000     0.000000
     200.00     0.000000     0.000000
     250.00     0.000000     0.000000
     300.00     0.000000     0.000000
     350.00     0.000000     0.000000
     400.00     0.000000     0.000000
     450.00     0.000000     0.000000
     500.00     0.000000     0.000000
     550.00     0.000000     0.000000
     600.00     0.000000     0.000000
     650.00     0.000000     0.000000
     700.00     0.000000     0.000000
     750.00     0.000000     0.000000
     800.00     0.000000     0.000000
     850.00     0.000000     0.000000
     900.00     0.000000     0.000000
     950.00     0.000000     0.000000
    1000.00     0.000000     0.000000
```

Figure B.5. Snapshot of .btc file.

```
filetype = meteo_on_computational_grid
NODATA_value = -999.000
n_quantity = 3
quantity1 = x_wind
quantity2 = y_wind
quantity3 = air_pressure
unit1 = m s-1
unit2 = m s-1
unit3 = Pa
TIME = 0.00000 minutes since 2020-08-05 00:00:00 +00:00
0.00 0.00 0.00 0.00 0.00 0.00 0.00 0.00 0.00 0.00 0.00
0.00 0.00 0.00 0.00 0.00 0.00 0.00 0.00 0.00 0.00 0.00
0.00 0.00 0.00 0.00 0.00 0.00 0.00 0.00 0.00 0.00 0.00
0.00 0.00 0.00 0.00 0.00 0.00 0.00 0.00 0.00 0.00 0.00
0.00 0.00 0.00 0.00 0.00 0.00 0.00 0.00 0.00 0.00 0.00
0.00 0.00 0.00 0.00 0.00 0.00 0.00 0.00 0.00 0.00 0.00
0.00 0.00 0.00 0.00 0.00 0.00 0.00 0.00 0.00 0.00 0.00
0.00 0.00 0.00 0.00 0.00 0.00 0.00 0.00 0.00 0.00 0.00
0.00 0.00 0.00 0.00 0.00 0.00 0.00 0.00 0.00 0.00 0.00
0.00 0.00 0.00 0.00 0.00 0.00 0.00 0.00 0.00 0.00 0.00
0.00 0.00 0.00 0.00 0.00 0.00 0.00 0.00 0.00 0.00 0.00
100910.00 100910.00 100910.00 100910.00 100910.00 100910.00 100910.00 100910.00 100910.00 100910.00 100910.00
100910.00 100910.00 100910.00 100910.00 100910.00 100910.00 100910.00 100910.00 100910.00 100910.00 100910.00
100910.00 100910.00 100910.00 100910.00 100910.00 100910.00 100910.00 100910.00 100910.00 100910.00 100910.00
100910.00 100910.00 100910.00 100910.00 100910.00 100910.00 100910.00 100910.00 100910.00 100910.00 100910.00
100910.00 100910.00 100910.00 100910.00 100910.00 100910.00 100910.00 100910.00 100910.00 100910.00 100910.00
100910.00 100910.00 100910.00 100910.00 100910.00 100910.00 100910.00 100910.00 100910.00 100910.00 100910.00
```

Figure B.6. Snapshot of .wnd file.

Further validation figure

In this appendix validation results for Test2, Test3, Test4, Test5 are reported.

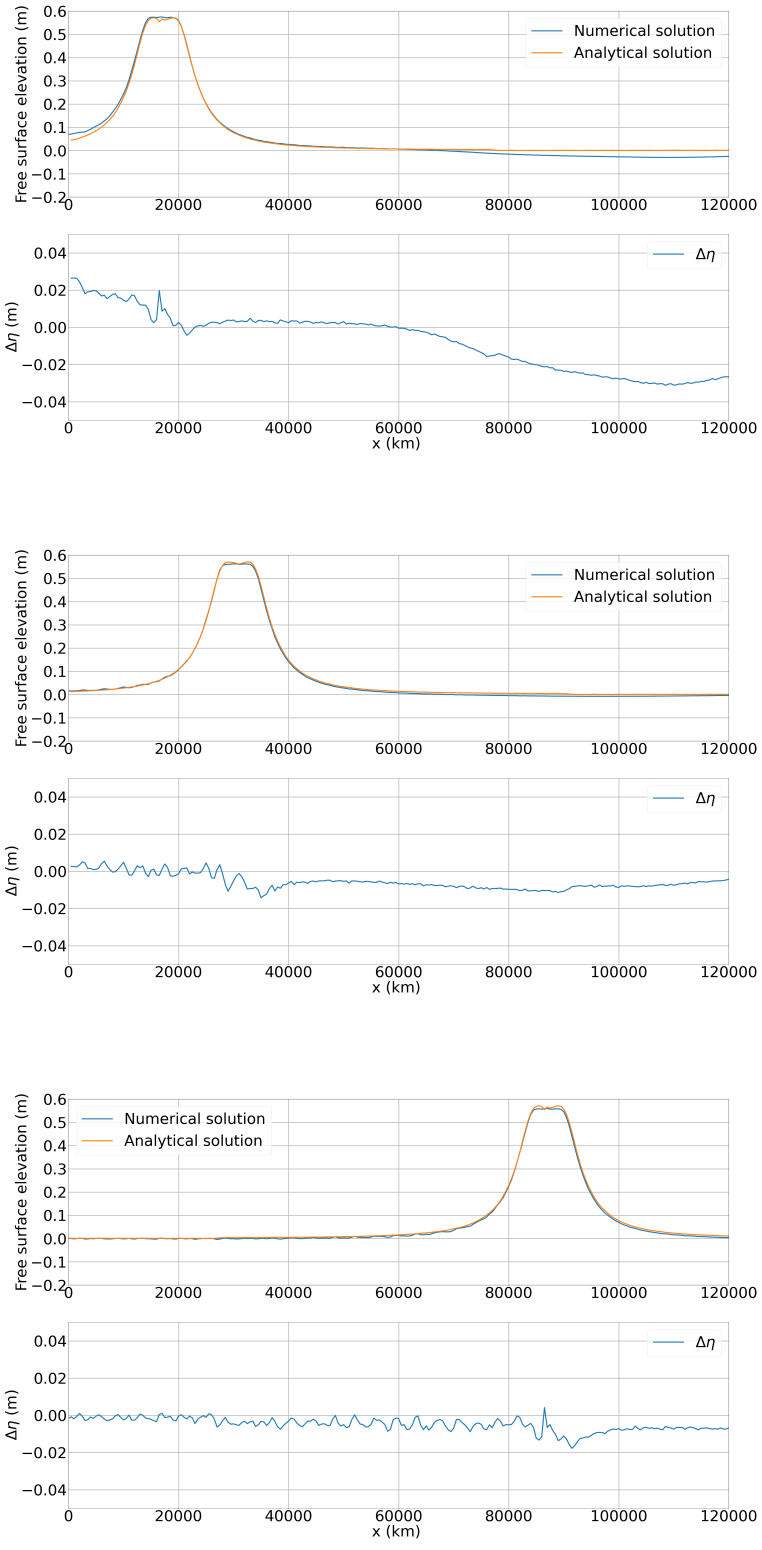

Figure C.1. Test2 result obtained for y = 0 km for t = 115, 138.3 and 235 minutes

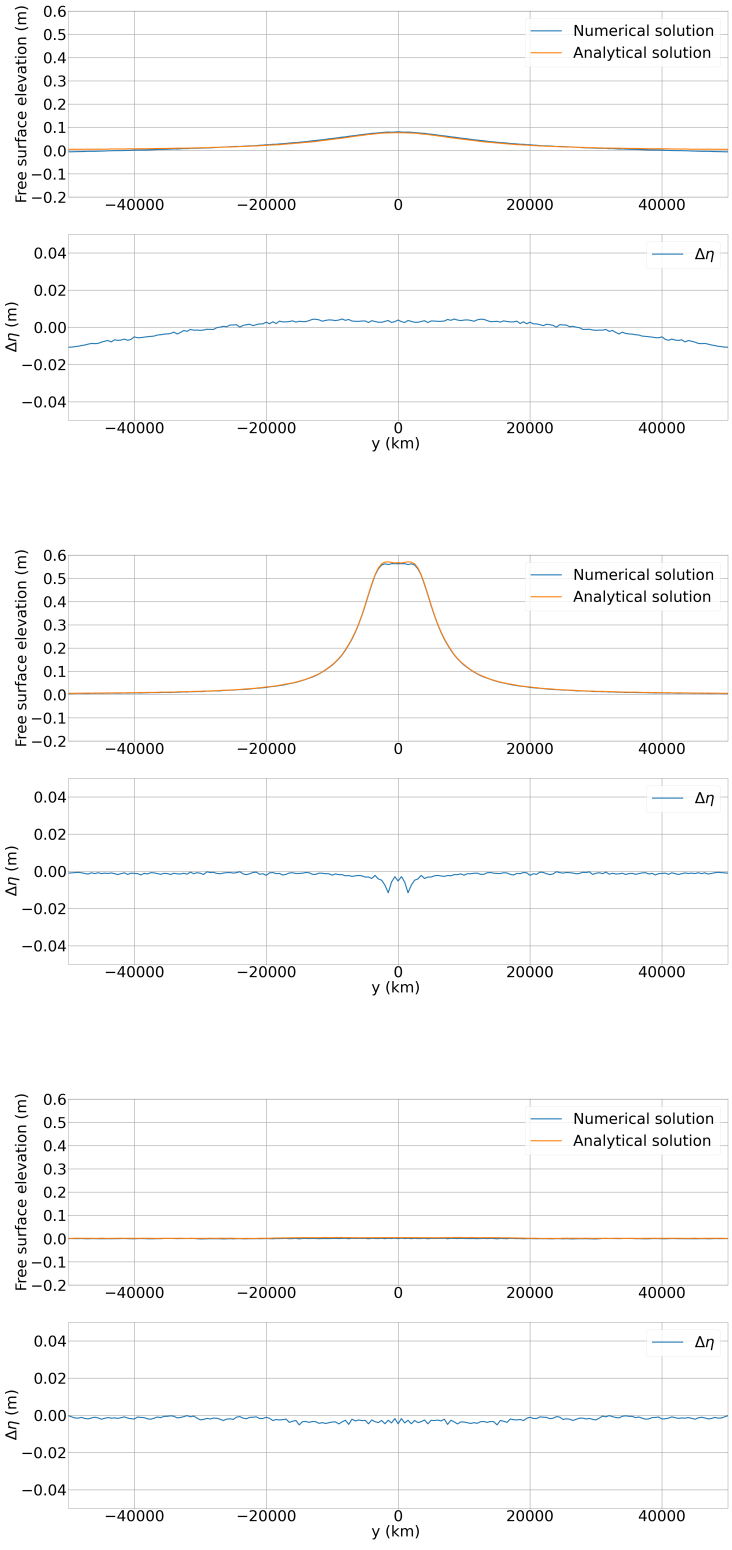

Figure C.2. Test2 result obtained for x = 30 km for t = 115, 138.3 and 235 minutes

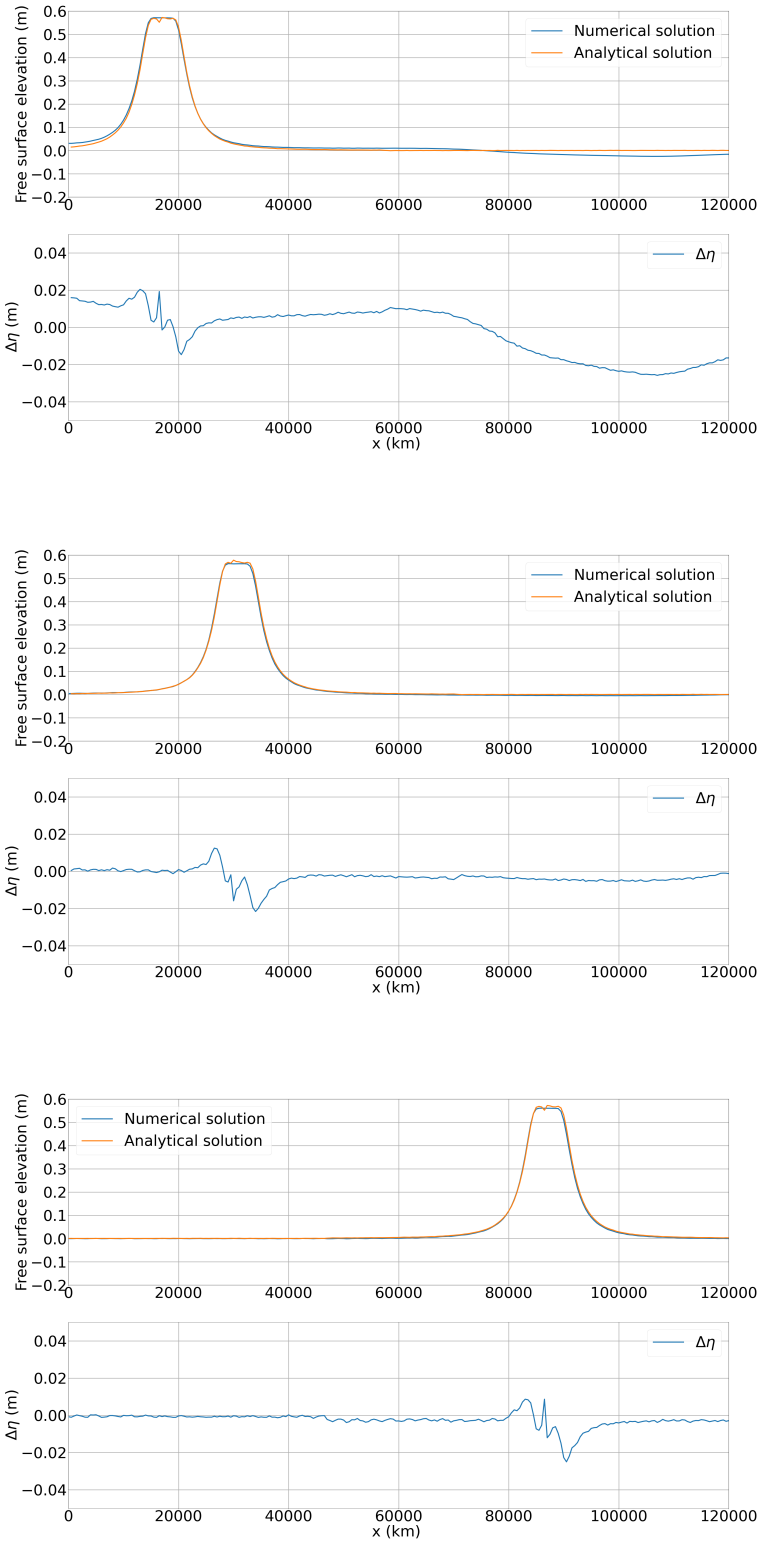

Figure C.3. Test3 result obtained for y = 0 km for t = 115, 138.3 and 235 minutes

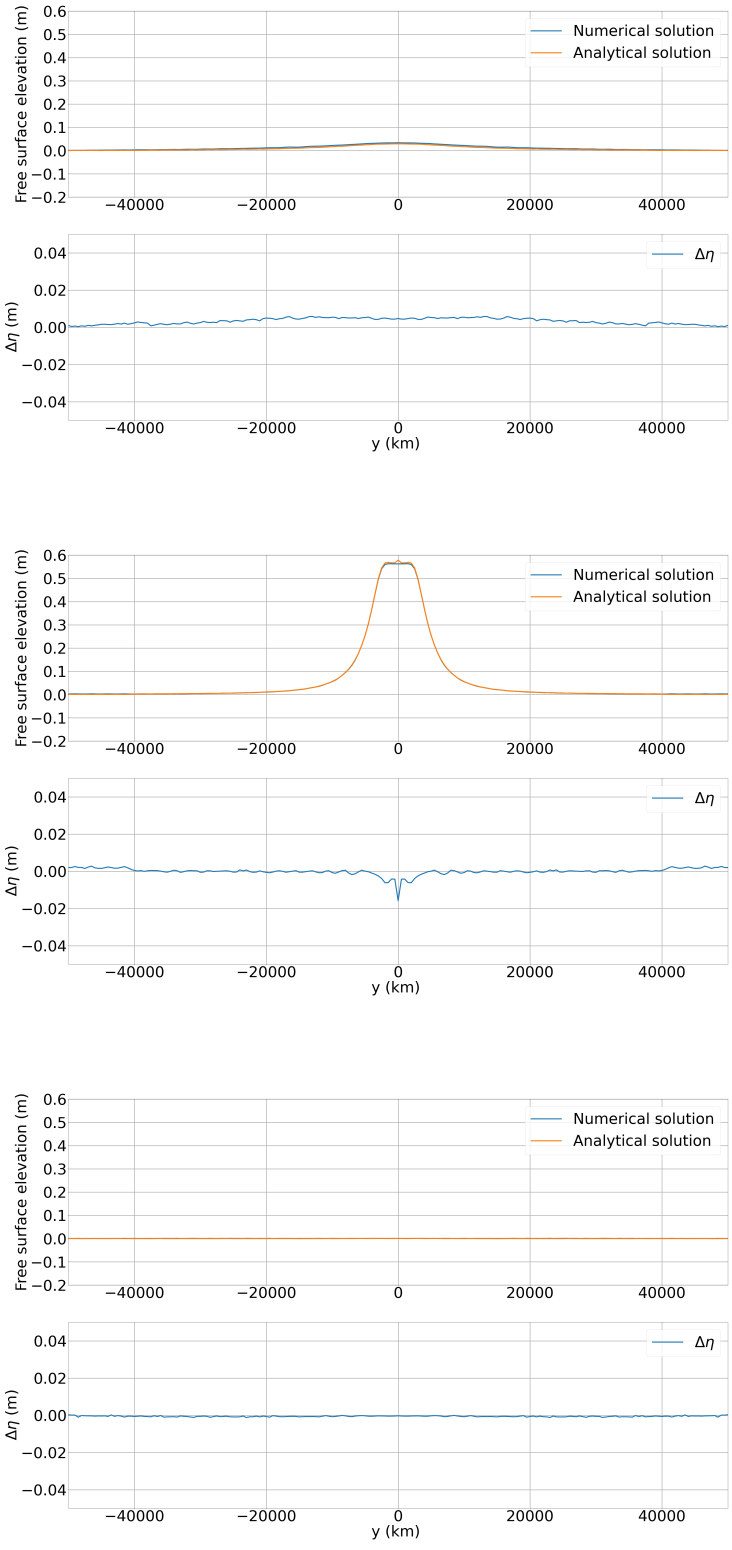

Figure C.4. Test3 result obtained for x = 30 km for t = 115, 138.3 and 235 minutes

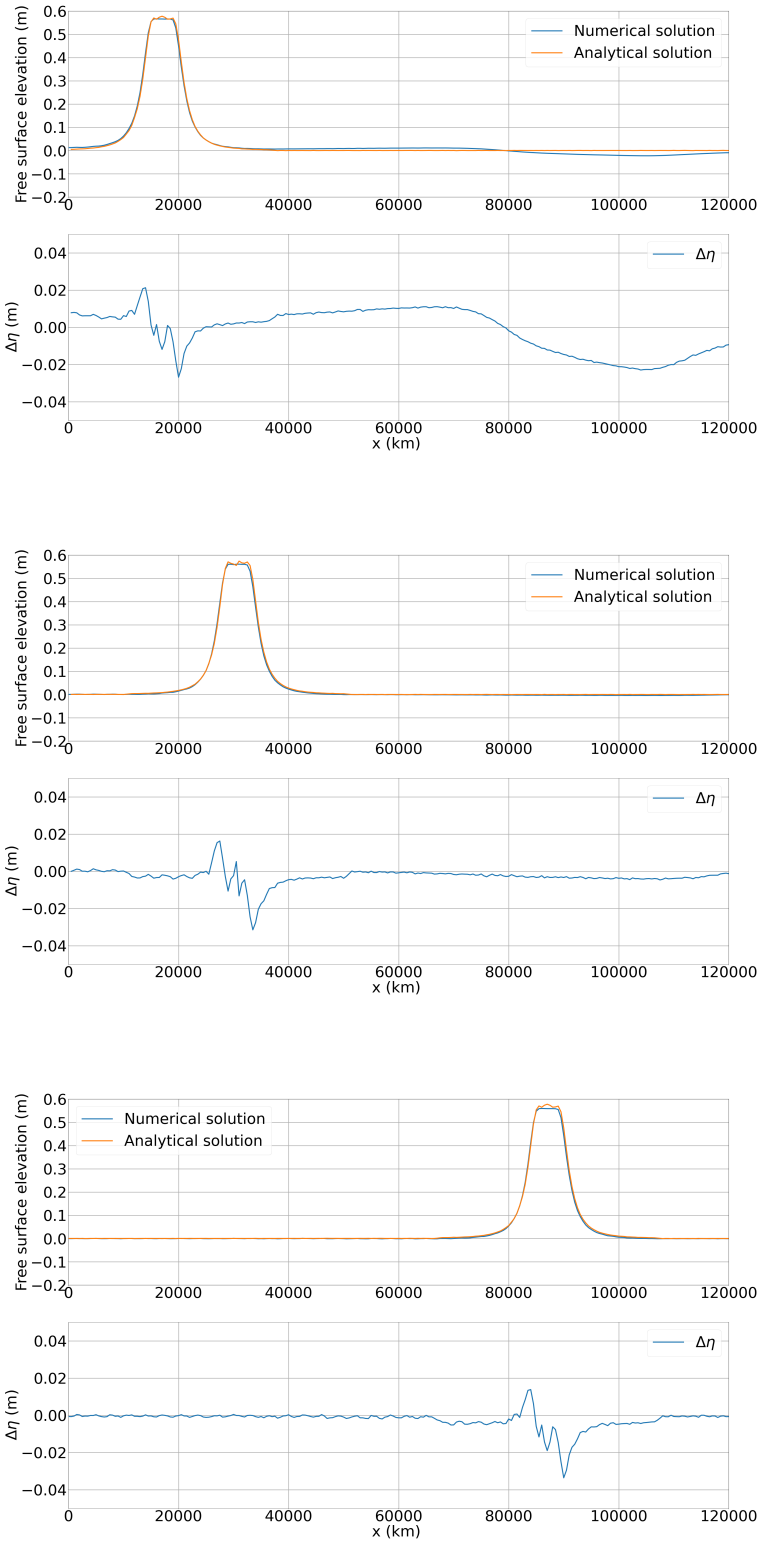

Figure C.5. Test4 result obtained for y = 0 km for t = 115, 138.3 and 235 minutes

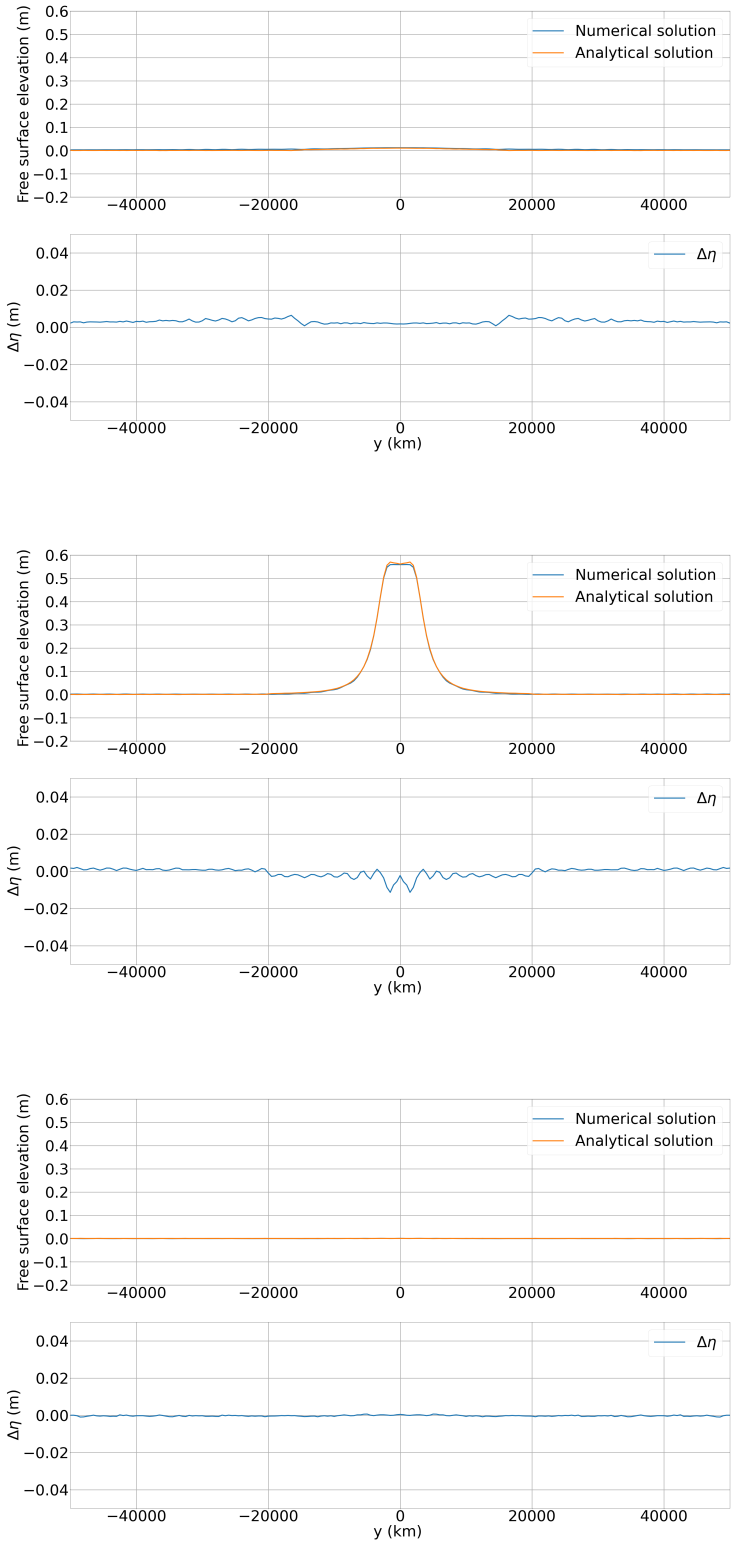

Figure C.6. Test4 result obtained for x = 30 km for t = 115, 138.3 and 235 minutes

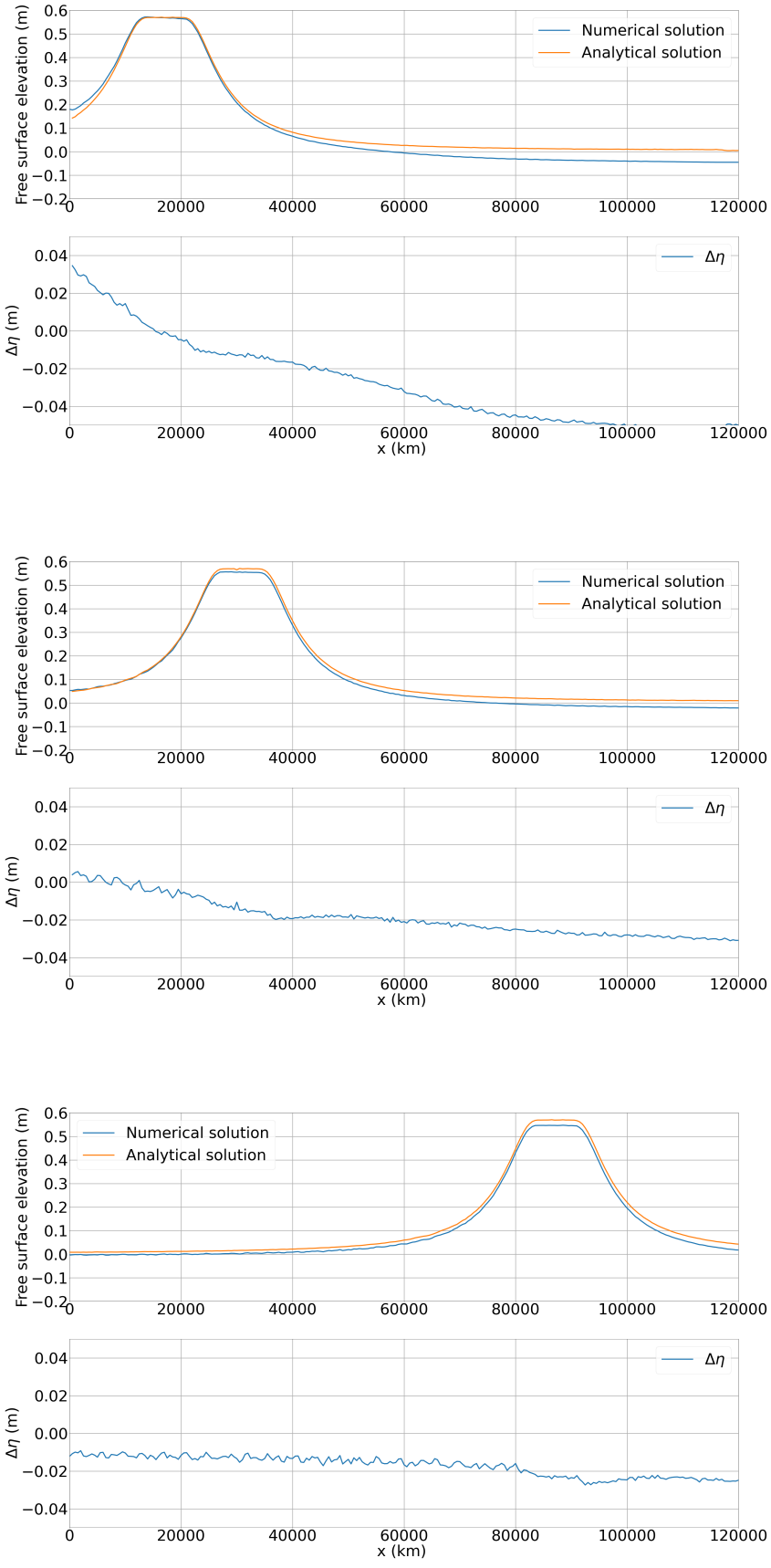

Figure C.7. Test5 result obtained for y = 0 km for t = 115, 138.3 and 235 minutes

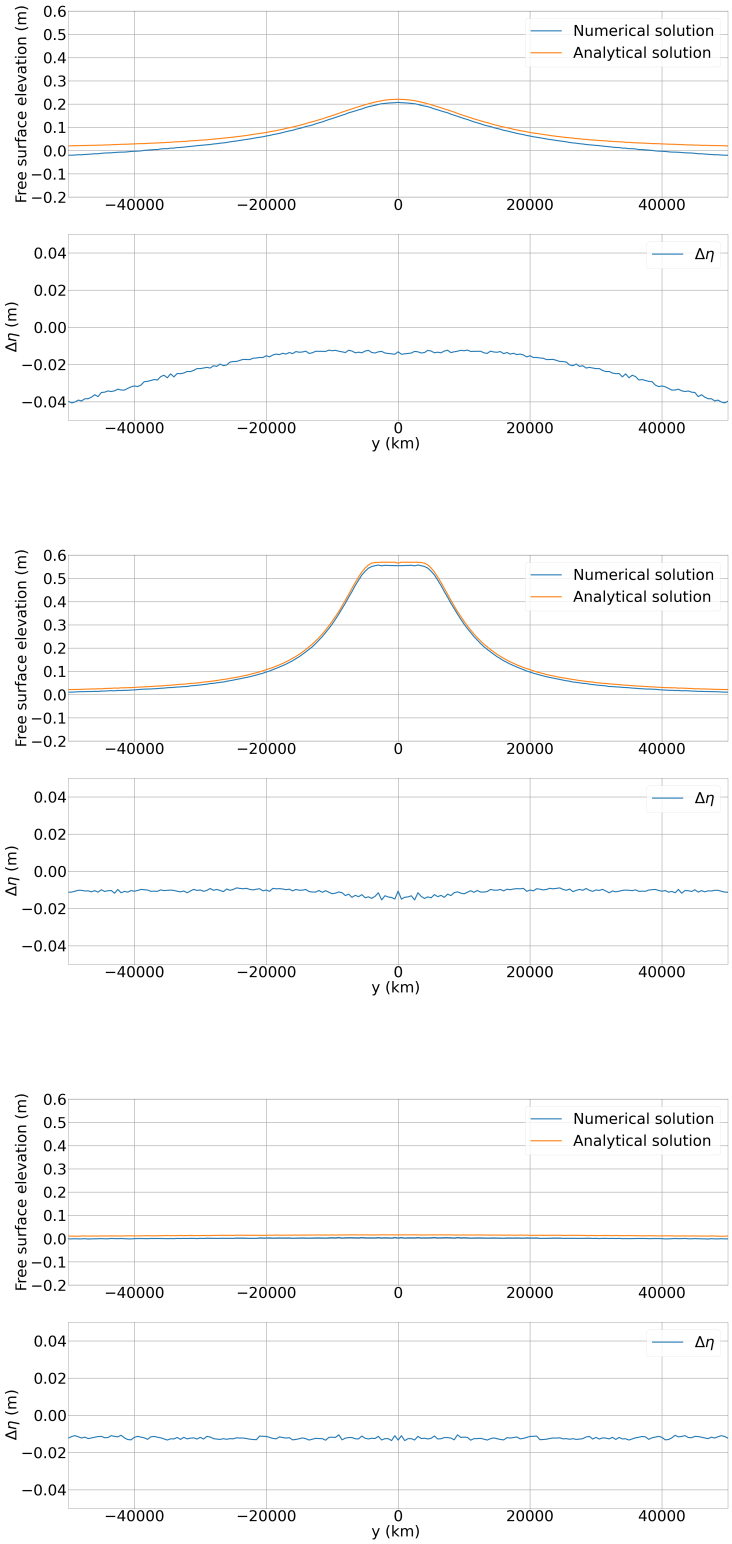

Figure C.8. Test5 result obtained for x = 30 km for t = 115, 138.3 and 235 minutes